Anisotropic Strain Rate Sensitive and Continuum Damage Coupled Plasticity Model: An Application for Magnesium AZ31B

by

Sari Kassar

A thesis submitted in partial fulfillment
of the requirements for the degree of
Master of Science in Engineering
(Mechanical Engineering)
in the University of Michigan–Dearborn
2018

Master's Thesis Committee:

Assistant Professor Georges Y. Ayoub, Co-chair
Professor Hong-Tae Kang, Co-chair
Professor Ghassan Kridli
Professor Pankaj Mallick
Assistant Professor Tanjore V. Jayaraman

DEDICATION

To my father George and mother Saada,
family and friends

ACKNOWLEDGEMENTS

This work was done during the years 2017-2018 as a graduate student research assistant at the College of Engineering and Computer Science at the University of Michigan – Dearborn.

I owe a great debt of gratitude to my research advisor Dr. Georges Y. Ayoub. He has served me a lifetime opportunity to dig deeper into the field of continuum mechanics and become a qualified and trained researcher. Without his guidance, this achievement would not have been possible.

I am deeply grateful to Dr. Hong-Tae Kang for serving as co-advisor on this research proceeding.

Thanks are also due to Dr. Ghassan T. Kridli, Dr. Pankaj Mallick and Dr. Tanjore V. Jayaraman for serving on my advisory committee.

TABLE OF CONTENTS

LIST OF FIGURES

LIST OF APPENDICES

ABSTRACT

In this work, an anisotropic and time-dependent damage-coupled plasticity model is written under finite strain formulation to describe the mechanical behavior of ductile materials. The model is formulated in arbitrary coordinate space to accommodate simulation of proportional and non-proportional 3D loadings. A phenomenological continuum damage mechanics approach is suggested to model the material mechanical behavior and anisotropic damage beyond the post-necking region up to fracture. The developed mathematical model scheme captures the strain rate effect on the material's mechanical response and better approximates the yield stress, ultimate tensile strength and the strain to fracture. This thesis also presents an implicit time integration method for the anisotropic time-dependent model. Magnesium alloys are the lightest structural metals and therefore are potential candidates for use in stamped automotive panels. Thus, the prediction capability of the model is validated by comparing the numerical predictions to the uniaxial tensile experiments of TRC sheets of Mg AZ31B Alloy. The comparisons between the numerical predictions and the experimental results show fair agreement over a multitude of strain rates and temperatures.

CHAPTER 1
INTRODUCTION

1.1 Engineering Background

Automotive manufacturers express high interest in sheet metal forming processes for high volume production vehicles. With tightened constraints on fuel efficiency and emissions, light-weighting has become crucial in the industry. This brings about an aggressive search for non-customary materials. The transition from steel to aluminum in the Ford F-150 truck declares an ideal example which hints to the need of innovative engineering methods to overcome material handling and manufacturing process challenges. Corrosion resistance, durability and recyclability are key factors of consideration for manufacturers. Material ductility and ease of machining are of critical importance in stamping, a plastic deformation process of sheet metal. Fortunately, some aluminum alloys have shown capability of providing such characteristics, and their use has been specifically attributed to their high strength-to-weight ratio compared to steel. This has enabled manufacturers to reduce the overall mass of their vehicles and achieve desired gas economy goals. Other alloys such as magnesium show highest strength-to-weight ratio of all structural materials; those are up to 33% lighter than aluminum and 75% lighter than steel. As the search for lighter alloys continues, new challenges arise for manufacturers when it comes to analyzing new material behavior and acquiring necessary tooling. Certain sheet metal characteristics such as anisotropy, spring-back and wrinkling hinder the ease of material handling and limit the formability of most alloys. Overall, such effects require attentive consideration and are often mitigated with the help of computer aided design and engineering. In current days, research engineers are constantly involved in enhancing their material characterization techniques. This serves to increase efficiency in manufacturing as it slashes production costs and improves product quality. While this research has shown considerable progress, there is yet a need of developing accurate prediction models for non-traditionally stamped ductile alloys. Fig. 1.1 below shows a magnesium sheet metal part manufactured by thermo-forming, where the sheets are heated to 842 degrees Fahrenheit and then placed in air-pressure dies to form the panels, a first in the industry by GM.

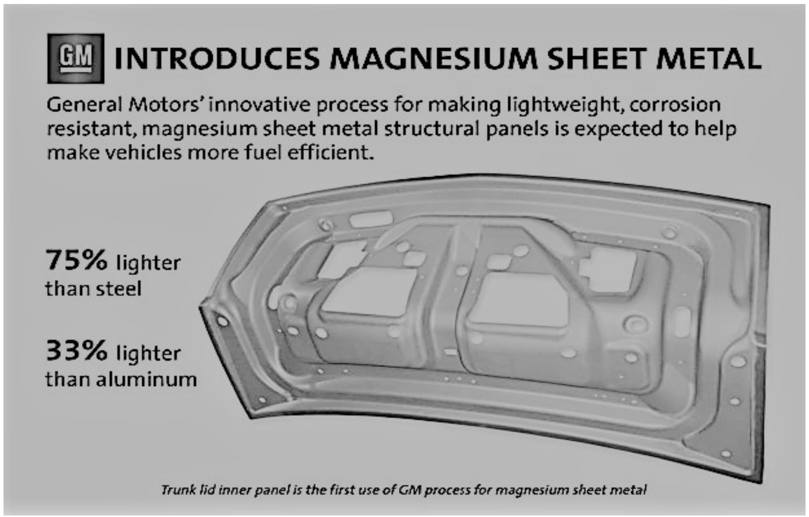

Fig. 1.1 – Thermo-formed Magnesium Panel – General Motors
(obtained from www.automotive.com)

1.2 Problem Statement

The study of ductile fracture is of primary importance in sheet metal forming. As a plastic deformation process, engineers need to predict the onset of necking and fracture of the formed alloy. The need is evident for a numerical tool which helps approximate the mechanical properties of the material in its elastic and plastic (hardening and softening) regions. In the modeling, it is essential to incorporate formulations which account for anisotropy to describe the directional dependence of material properties. In order to model the post-necking region of the material, damage-coupled plasticity is considered. In general, material damage is regarded as the deterioration of the material due to the formation of dislocations, micro-cracks and other material defects (Fonseka and Krajcinovic 1981). To quantify this damage, a scalar variable (isotropic) or a tensor (anisotropic) can be used to assess the degree of damage in the subjected material. In the literature search of this thesis, some of the ductile fracture criteria presented are intended for micro-mechanical analysis. Those did account for damage in materials by proposing porosity variables or scalar damage accumulation rules. In this work, however, it is sought to derive macro-scale level model based on the mechanics of a continuous medium. This is due to the flexibility that this approach can offer in acknowledging the material's anisotropic behavior. Thus, the theory of continuum damage mechanics (CDM) is of interest to this study. Continuum damage mechanics is a theory based on the thermodynamics of irreversible processes to model overall material degradation without reference to physical microstructures (Lemaitre 1996). Being a branch of continuum mechanics, the approach can effectively incorporate damage evolution equations in continuum plasticity models. In the automotive industry, cold-stamping is a common process to shape the sheets of metal. When considering use of non-conventionally stamped alloys for the sake of light-weighting, operators are faced with the unfeasibility of cold-stamping, particularly for the case of magnesium (Robson 2015). This unfeasibility is due to the low ductility, limited deformation systems and strong basal texture (Doege and Dröder 2001; Rodriguez et al. 2013) that the material exhibits at cold (room) temperatures. Thus, forming of magnesium requires elevated temperatures; the employment of magnesium, for instance, justifies the need of a model capable of modeling its behavior at both cold and elevated temperatures. At high temperatures, a challenge is present in which the material becomes highly sensitive to strain rate. As such, the work in this thesis seeks to address the rate-dependency (visco-plasticity) and temperature influence. Overall, the developed numerical ductile fracture model in this work is made to account for such complex material behaviors. Subsequently, the goal is to optimize the visco-plastic model for the use in commercial finite-element software which can be done by user subroutine implementation. One particular aspect involving this implementation is the need for a computationally efficient and robust iterative integration scheme for the solution of the non-linear rate equations; thus, ensuring accurate numerical prediction while preserving computational efficiency is yet another challenge. Hence, the contribution of this thesis is manifested in presenting a numerical model and technique which **(a)** accounts for material anisotropy, **(b)** responds to changes in strain rate and **(c)** captures the damage influence on post-necking behavior of ductile alloys.

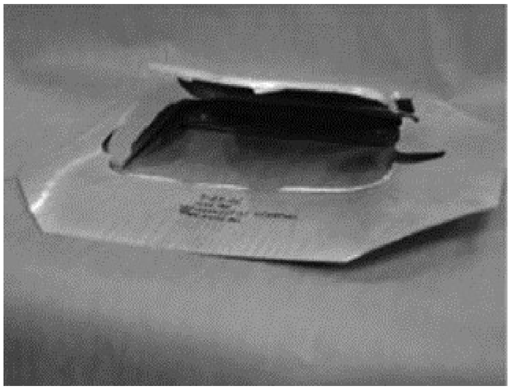

Fig. 1.2 – Mg AZ31B Cold-Stamping
(obtained from Powell, Krajewski, and Luo 2010)

1.3 Fundamental and Theoretical Knowledge

This thesis work encompasses fundamental elements in the theory of plasticity and damage mechanics. In this section, an overview of the basic principles in those theories is presented to the reader for the analysis of fracture in ductile metals. The concept of a continuous medium is explained, and highlights from theory of plasticity are included.

1.3.1 Overview of a Continuous Medium

In a continuous medium, researchers are involved with the study of stress, deformation and flow in solids. For a hypothetical material, the molecular structure is disregarded, and the possible presence of gaps is ignored. Mathematically, continuous nature of functions and derivatives is assumed, except at interior surfaces where regions of continuity are separated (Malvern 1969). The theory can assume two further assumptions for constitutive modeling: the independence of material point properties from both position (homogeneity) and direction (isotropy). The use of such mathematical theory can assist researchers with quantitative analysis over the concept of continuity. While the theory might not genuinely describe the true nature of matter, the applicability and usefulness of a continuous medium can be assessed and validated by experiments (as will be assessed in this work) or comparison to higher level theories (Malvern 1969).

1.3.2 Theory of Plasticity

It is commonly observed for a ductile material to exhibit two modes of mechanical behavior: elastic and plastic deformation. In this section, the aim is to discuss the fundamental theory for the description of plasticity in materials. In constitutive modeling and according to the flow theory, the plasticity of a material is defined by a yield criterion, a flow rule, an isotropic/kinematic hardening rule and a loading condition (Wu 2005).

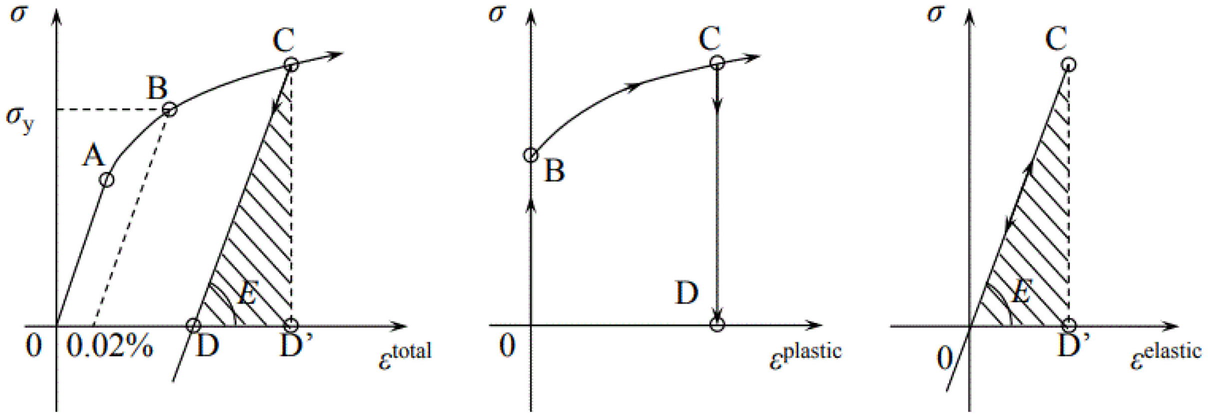

Fig. 1.3 – Elastic and Plastic Regions of a Stress-Strain Curve
(adapted and modified from https://ocw.mit.edu))

The yield stress is a unique material constant which identifies the limit for applied stress beyond which material plasticity is activated; however, this is more relevant to the uniaxial case (as in Fig. 1.3). In an arbitrary coordinate system (3-D), a yield criterion is implemented and can be defined as a potential stress function of a second order tensor which sets the boundaries between a material's elastic and plastic regions in the stress space; the six components of the stress tensor constitute yielding of the material. The representation of such a function is typically portrayed by a yield surface (yield locus).

The following conditions are those of a plastic potential function g which describes the material behavior states accordingly:

- $g(\sigma_{ij}) < 0$ denotes an elastic state
- $g(\sigma_{ij}) = 0$ denotes a plastic state
- $g(\sigma_{ij}) > 0$ denotes an inadmissible state

Generally, the determination of yield surfaces can be done experimentally by varying loading conditions. It is essential for a yield criterion to be applicable even in cases such as that for a rotation of the stress coordinate system occurring due to a non-proportional loading. This defines a starting point for the determination of a yield criterion. It is acknowledged that the hydrostatic component of a stress tensor does not cause yielding in a material which is plastically incompressible, specifically metals (Wu 2005). Only the deviatoric stress, often denoted as σ', causes plastic flow in a material, accounting for the shear stress of the stress tensor. With this foundation, and for an isotropic solid, the yield criterion is often associated with the invariants of the deviatoric component of the stress tensor, specifically the second invariant, which hints to the J-2 plasticity theory of von Mises.

When the plasticity of a material is activated, it becomes necessary to specify a strain increment. This is achieved with the implementation of a flow rule. For this study, the case is that of an associated flow rule. From the early literature, Prandtl and Reuss use the plastic strain increment $d\varepsilon_{ij}^{p}$ to propose a plastic evolution rate (Malvern 1969) such that:

$$d\varepsilon_{ij}^{p} = d\lambda T_{ij}^{'} \tag{1.1}$$

where $d\lambda$ is a scalar multiplier of proportionality and $T_{ij}^{'}$ is the Newtonian viscosity function, for a perfectly plastic material idealization. Note that for a perfectly plastic material, the yield surface maintains its original shape. On another note, experimental findings and the normality rule (Drucker's postulate) require that for a convex yield surface, the plastic strain increment must be normal to the surface (Malvern 1969; Ohashi, Kawashima, and Yokochi 1975; Phillips and Moon 1977).

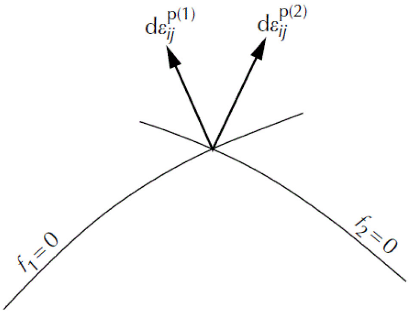

Fig. 1.4 – Plastic Strain Increment Normality
(adapted from Wu 2005)

Basing our study on a hardening material and a general yielding condition, the plastic rate of evolution can be written according to the normality rule, such that:

$$d\varepsilon_{ij}^{p} = d\lambda \frac{\partial g}{\partial \sigma_{ij}} \tag{1.2}$$

where $d\lambda$ is a scalar plastic multiplier describing the accumulation of plastic hardening, and g is the plastic potential function which describes a surface in the stress space (Krabbenhoft 2002). With the employment of an associated flow rule, g can be approximated to the yield function f, which reduces the plastic increment to:

$$d\varepsilon_{ij}^{p} = d\lambda \frac{\partial f}{\partial \sigma_{ij}} \tag{1.3}$$

For the multiaxial case, and for a strain hardening material, it becomes necessary to embed this phenomenon in the form of a rule. This is because yield surface can undergo expansion and translation (Wu 2005) in the presence of strain hardening and upon continued deformation. The surface expansion is commonly attributed as isotropic hardening where the size of the yield surface uniformly increases in radius (as in Fig. 1.5) and indicates a subsequently higher yield value. The surface translation, however, is known as kinematic hardening where the center of the yield surface is shifted, leaving no effect on its size (as in Fig. 1.7).

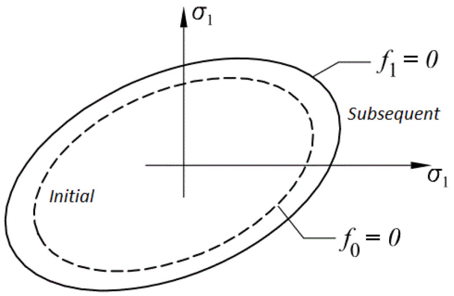

Fig. 1.5 – Subsequent Yield Surface – Isotropic Hardening
(adapted and modified from Krabbenhoft 2002)

In the case of isotropic hardening, the yield function can be expressed as follows:

$$f(\sigma_{ij}) - R^2 = 0 \tag{1.4}$$

where R is a variable representing the size (radius) for the subsequent yield surface, occurring after the expansion of the initial yield surface.

Before the kinematic hardening rule is explained, it is important to understand a notable phenomenon known as the Bauschinger effect. This phenomenon is observed in the decrease of material strength when the deformation (loading) path is reversed (Atkinson, Brown, and Stobbs 1974). According to (Zhou and LeSar 2012), it has been shown in their analysis of dislocation dynamics that the reverse motion of pileups and the collapse of misfit dislocation are responsible for this observed effect. In Fig. 1.6, the effect is shown on a stress-strain curve, pointing out to a reduced strength in the reversely loaded direction.

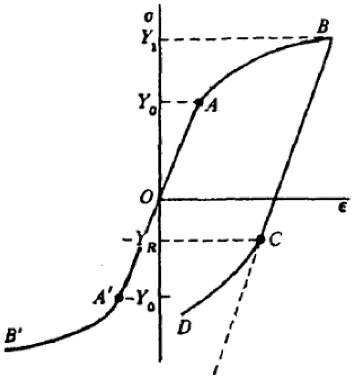

Fig. 1.6 – Stress Strain curve illustrating the Bauschinger Effect
(adapted from Malvern 1969)

Hence, the introduction of a kinematic hardening rule becomes necessary to account for this effect. This has been pioneered by (Prager 1955). The concept was later applied to the arbitrary stress space by (Hodge 1956) where the subsequent yield surface can be written such that:

$$f(\sigma_{ij} - \alpha_{ij}) = 0 \tag{1.5}$$

where α_{ij} is the back stress which quantifies the translation from the initial yield surface to the subsequent surface. The effect is shown below in Fig 1.7 in the stress space.

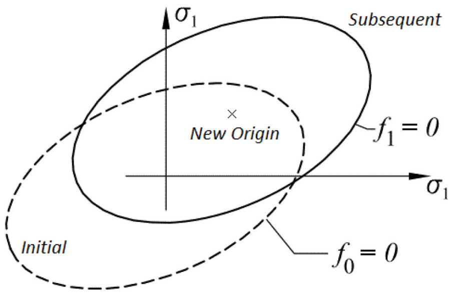

Fig. 1.7 – Subsequent Yield Surface – Kinematic Hardening
(adapted and modified from Krabbenhoft 2002)

1.3.3 Yield Criteria

As discussed earlier, the yielding criteria for plastically incompressible materials does not depend on the spherical component of the stress tensor. Of the most commonly known yielding criterion is the Tresca criterion which defines yielding as a result of one of the shear stresses exceeding a critical limit. Another is the von Mises criterion which predicts yielding by accounting for the three principal shear stresses of the stress tensor. The von Mises criterion is capable of predicting yielding based on any of the principal stress exceeding the critical limit while adjusting for the other stresses. In other words, it accounts for the combination of principal stresses that would cause the yielding in the material (Krabbenhoft 2002).

1.3.3.1 Tresca (Isotropic)

Tresca's criterion may simply be written knowing that yielding occurs when the maximum shear stress of a material equals the maximum shear stress at yielding for uniaxial tension, such that:

$$f(\sigma'_{ij}) = \sigma_{eq} - k = \sigma_{eq} - \frac{\sigma_y}{2} \tag{1.6}$$

where σ_y is the yield stress for the uniaxial case and can be determined with a simple tension test.

1.3.3.2 von Mises (Isotropic)

The von Mises criterion occurs when the distortional strain energy reaches a value which causes yielding in a simple tension test, a value which is independent of any coordinate system (Budynas and Nisbett 2008). A modified version of the criterion uses the second invariant of the deviatoric component of the stress tensor J-2 and is equal to the negative half inner product of the deviatoric stress tensor contracted on both indices. The yield function can be written below as:

$$f(J_2) - k^2 = 0 \tag{1.7}$$

where k is the critical yield limit.

1.3.3.3 Hill's Quadratic Yield Criterion (Anisotropic)

We introduce Hill's quadratic yield criterion due to its relevance to sheet metal and the study of this thesis. The criterion assumes that yielding is independent of the spherical component of the stress tensor. In its isotropic case, Hill's quadratic equation reduces to the von Mises yield criterion depending on the fixed material parameters F, G, H, L, M and N as shown in the below yield function (Hill 1948):

$$f(\sigma_{ij}) = \left[F\left(\sigma_y - \sigma_z\right)^2 + G\left(\sigma_z - \sigma_x\right)^2 + H\left(\sigma_x - \sigma_y\right)^2 + 2L\sigma_{yz}^2 + 2M\sigma_{zx}^2 + 2N\sigma_{xy}^2 \right] = 1 \tag{1.8}$$

Hence, the von Mises criterion becomes a special case of the Hill criterion when the anisotropic coefficients are as follows:

- $F = G = H = 1$
- $L = M = N = 3F$

It is noteworthy that Hill's criterion does not assume the Bauschinger effect but considers the axes of anisotropy as reference (Wu 2005). For the case of sheet metal, the equation can be written in the plane space such that:

$$\left(G + H\right)\sigma_x^2 - 2H\sigma_x\sigma_y + \left(F + H\right)\sigma_y^2 + 2N\sigma_{xy}^2 = 1 \tag{1.9}$$

The parameters F, G, H and N can be determined experimentally using material tensile and shearing yield stresses. In this work, the Hill parameters are obtained for the alloy of interest. This concludes our study of yield criteria relevant to this thesis.

1.4 Thesis Scope and Objective

Fundamentally, this thesis explores some of the popular ductile fracture criteria used in today's industry. Examples of these criteria lie within the mathematically derived, micro-mechanical and the macro-mechanical analysis for the description of ductile damage in materials. An insight on the strain-based Mohr-Coulomb (M-C) criterion is provided, as it was extended for practical application to predict ductile fracture in metals with the dependency on the Lode angle and hydrostatic pressure (Bai and Wierzbicki 2010). The micro-mechanical approaches are highlighted by the Gurson-Tvergaard-Needleman (GTN) type models. In this thesis, the phenomenological CDM approach is employed based on the developments by the authors (Lemaitre, Cordebois, and Dufailly 1979; Chow, Yu, and Demeri 1997; Chow and Jie 2008) and is modified to account for the time-dependent behavior of common ductile alloys. The thesis work constitutes the following:

1. An anisotropic damage-coupled plasticity model is developed in arbitrary coordinate space for finite strains to accommodate simulation of non-proportional 3D loadings and fracture of ductile alloys which is of great interest for automotive stamping manufacturers
2. Plastic and damage multipliers are approximated with the incorporation of time dependent laws for plastic strain and overall damage accumulation to capture the strain rate effect on a material's plastic deformation behavior at elevated temperatures as well as controlling the damage response with respect to the material's damage and deformation mechanisms
3. An implicit time integration scheme is proposed for the solution of the model's equations based on the backward Euler method for multidimensional root finding
4. The constitutive model is implemented in MATLAB® and is validated for the uniaxial case using experimental stress-strain data obtained for TRC sheets of Mg AZ31B Alloy

1.5 Thesis Organization

This thesis contains five chapters and are described below:

Chapter One provides a background of the thesis topic, discusses sheet metal applications, provides an overview of some principles in continuum mechanics and plasticity and states the contribution of this research work.

Chapter Two presents a comprehensive literature review on the most commonly used ductile fracture criteria in today's industry to compare their features and limitations.

Chapter Three provides the equations of the anisotropic damage coupled plasticity model and highlights the time-dependent constitutive modifications to the equations of plasticity and damage accumulation. The chapter proposes a fully implicit time integration scheme for guaranteed solution stability and increased computational efficiency.

Chapter Four validates the numerical predictions of the model for the uniaxial case against the experimental data of Mg AZ31B Alloy. The chapter provides qualitative and quantitative attempts to assess the model's capability in capturing the stress strain response as well as accurately approximating the material's mechanical properties.

Chapter Five summarizes the contributions of the work done in this study and suggests future research heading.

1.6 References

Atkinson, J. D., L. M. Brown, and W. M. Stobbs. 1974. “The Work-Hardening of Copper-Silica: IV. The Bauschinger Effect and Plastic Relaxation.” *Philosophical Magazine* 30 (6): 1247–80. https://doi.org/10.1080/14786437408207280.

Bai, Yuanli, and Tomasz Wierzbicki. 2010. “Application of Extended Mohr-Coulomb Criterion to Ductile Fracture.” *International Journal of Fracture* 161 (1): 1–20. https://doi.org/10.1007/s10704-009-9422-8.

Budynas, RG, and JK Nisbett. 2008. *Shigley's Mechanical Engineering Design*. http://www.academia.edu/download/30923192/200103016.pdf.

Chow, C. L., L. G. Yu, and M. Y. Demeri. 1997. “A Unified Damage Approach for Predicting Forming Limit Diagrams.” *Journal of Engineering Materials and Technology* 119 (4). American Society of Mechanical Engineers: 346. https://doi.org/10.1115/1.2812269.

Chow, C.L., and M. Jie. 2008. “Anisotropic Damage-Coupled Sheet Metal Forming Limit Analysis.” *International Journal of Damage Mechanics* 18 (4): 371–92. https://doi.org/10.1177/1056789508097548.

Doege, E., and K. Dröder. 2001. “Sheet Metal Forming of Magnesium Wrought Alloys—formability and Process Technology.” *Journal of Materials Processing Technology* 115 (August): 14–19. https://doi.org/http://dx.doi.org.libaccess.lib.mcmaster.ca/10.1016/S0924-0136(01)00760-9.

Fonseka, G. U., and D. Krajcinovic. 1981. “The Continuous Damage Theory of Brittle Materials, Part 2: Uniaxial and Plane Response Modes.” *Journal of Applied Mechanics* 48 (4): 816. https://doi.org/10.1115/1.3157740.

Hill, R. 1948. “A Theory of the Yielding and Plastic Flow of Anisotropic Metals.” *Proceedings of the Royal Society A: Mathematical, Physical and Engineering Sciences* 193 (1033). The Royal Society: 281–97. https://doi.org/10.1098/rspa.1948.0045.

Hodge, P. G. 1956. “Piecewise Linear Plasticity.” *Proceedings 9th International Congress of Applied Mechanics* , no. Chap. 11: 65.

Kristian Krabbenhoft. 2002. “Basic Computational Plasticity.” Homes.civil.aau.dk. 2002. http://homes.civil.aau.dk/lda/continuum/plast.pdf.

Lemaitre, J., J.P. Cordebois, and J. Dufailly. 1979. “Sur Le Couplage En-Dommagement-Elasticite.” *Compte-Rendu a I'Academie Des Sciences Paris*, 288.

Lemaitre, Jean. 1996. *A Course on Damage Mechanics*. Berlin, Heidelberg: Springer Berlin Heidelberg. https://doi.org/10.1007/978-3-642-18255-6.

Malvern, LE. 1969. *Introduction to the Mechanics of a Continuous Medium*. https://trid.trb.org/view.aspx?id=199874.

Ohashi, Y., K. Kawashima, and T. Yokochi. 1975. “Anisotropy due to Plastic Deformation of Initially Isotropic Mild Steel and Its Analytical Formulation.” *Journal of the Mechanics and*

Physics of Solids 23 (4–5): 277–94. https://doi.org/10.1016/0022-5096(75)90029-0.

Phillips, A., and H. Moon. 1977. "An Experimental Investigation Concerning Yield Surfaces and Loading Surfaces." *Acta Mechanica* 27 (1–4): 91–102. https://doi.org/10.1007/BF01180078.

Prager, William. 1955. "The Theory of Plasticity: A Survey of Recent Achievements." *Proceedings of the Institution of Mechanical Engineers* 169 (1): 41–57. https://doi.org/10.1243/PIME_PROC_1955_169_015_02.

Robson, J. D. 2015. "Critical Assessment 9: Wrought Magnesium Alloys." *Materials Science and Technology* 31 (3): 257–64. https://doi.org/10.1179/1743284714Y.0000000683.

Rodriguez, A. K., G. Kridli, G Ayoub, and H. Zbib. 2013. "Effects of the Strain Rate and Temperature on the Microstructural Evolution of Twin-Rolled Cast Wrought AZ31B Alloys Sheets." *Journal of Materials Engineering and Performance* 22 (10). Springer US: 3115–25. https://doi.org/10.1007/s11665-013-0598-8.

Wu, H C. 2005. *Continuum Mechanics and Plasticity*. *New York*. https://doi.org/doi:10.1201/9780203491997.ch6.

Zhou, Caizhi, and Richard LeSar. 2012. "Dislocation Dynamics Simulations of the Bauschinger Effect in Metallic Thin Films." *Computational Materials Science* 54 (March). Elsevier: 350–55. https://doi.org/10.1016/J.COMMATSCI.2011.09.031.

CHAPTER 2
LITERATURE REVIEW

In this chapter, a comprehensive literature search is provided to highlight the developments in the study of ductile fracture of metals. Some of the commonly used criteria in today's industry are compared by their features and limitations. The survey reviews approaches including the GTN model, the Mohr-Coulomb criterion and the phenomenological CDM model.

2.1 Micromechanical Ductile Fracture Analysis

The micromechanical approach to modeling ductile fracture is described by the nucleation, growth and coalescence of micro-voids. In literature, micromechanical ductile fracture prediction modeling is classified into uncoupled (McClintock-Rice-Tracey) and coupled (Gurson-Tvergaard-Needleman) micromechanical models.

2.1.1 Uncoupled Micromechanical Modeling

The initial models corresponding to ductile damage were pioneered by (McClintock 1968) and (Rice and Tracey 1969) which described the growth of spherical holes (voids) in a material; stress triaxiality and plastic strain were assumed to induce ductile void growth. These models are often classified as uncoupled (Rakin et al. 2004), and it is assumed that the presence of voids does not affect the behavior of the material (Bauvineau et al., 1996), due to the non-interaction between isolated voids and adjacent voids in the early phases of ductile fracture. Thus, the incorporation of such interaction effect was neglected in initial finite element modeling (Miller and Anderson

1995). In their works, (Rice and Tracey 1969) study the enlargement of isolated spherical voids in a continuous medium. The authors assume the von Mises yield criterion, where they propose a critical void growth ratio for a non-hardening material, such that

$$\frac{\dot{R}}{R_0} = 0.283\exp\left(\frac{3\sigma_m}{2\sigma_0}\right)\dot{\varepsilon}_{eq}^{p} \tag{2.1}$$

where $\dot{R}$ is the mean void radius rate, R_0 is the initial void radius, σ_0 is the matrix yield stress and ε_{eq} is the equivalent von Mises strain. In order to establish a rupture criterion, a ratio $\left(\frac{R}{R_0}\right)_c$ can be used and considered as a material dependent parameter that defines a critical value corresponding to the critical growth of the void (Marino et al.,1985) and ultimately the point of fracture. The void growth formulations were later extended to account for strain hardening by the authors (Budiansky et al., 1982). Overall, no evolution for damage was assumed within the yield criterion. Moreover, the coalescence of an isolated void with adjacent void growth (softening) cannot be captured in this model (Besson 2010). Hence, the use of this model may then only be justified for detecting crack initiation (Rakin et al. 2004).

2.1.2 Coupled Micromechanical Modeling

With the limitation of the uncoupled model being identified, (Gurson 1977) incorporated a damage variable to include capturing the post-necking region (softening phase). Void volume fraction (or porosity) was used to quantify the damage in a perfectly plastic matrix (Besson 2010), which was done by defining a plastic yield function that incorporated the proposed porosity variable f, such that

$$\phi = \frac{\sigma_{eq}^2}{\sigma_0^2} + 2f\cosh\left(\frac{1}{2}\frac{\sigma_{kk}}{\sigma_0}\right) - 1 - f^2 \tag{2.2}$$

where σ_{kk} is the first invariant of the stress tensor. Having defined the yield function ϕ, the plastic strain rate $\dot{\varepsilon}_p$ can be defined according to the normality rule. As such, (Gurson 1977) defines the evolution of porosity (growth) based on mass conservation, such that

$$\dot{f} = (1-f)\,\mathrm{tr}\left(\dot{\varepsilon}_p\right) \tag{2.3}$$

which is dependent on $\dot{\varepsilon}_p$ that is determined by the yield surface.

Eventually, (Tvergaard and Needleman 1984) proposed a modification to the yield surface ϕ to have a better representation of experiments in such a way that additional parameters were added to describe the kinetics of void growth. The resulting model was since known as the Gurson-Tvergaard-Needleman (GTN) model. As such, the modified yield surface may be expressed as

$$\phi = \frac{\sigma_{eq}^2}{R^2} + 2q_1 f^* \cosh\left(\frac{1}{2} q_2 \frac{\sigma_{kk}}{\sigma_0}\right) - 1 - q_1^2 \left(f^*\right)^2 \tag{2.4}$$

where f is replaced by the effective porosity f^* for enhanced coalescence modeling. An additional assumption was made such that when f reaches a critical porosity value f_c, damage increases drastically due to void coalescence. Note that when f^* is zero, the yield surface is reduced to the von Mises surface.

The effective porosity may take the actual void volume fraction before the critical coalescence limit f_c is reached, after which f^* takes a different equation. We may summarize both cases in the function below

$$f^* = \begin{cases} f & \text{if } f \le f_c \\ f_c + \left(\dfrac{1}{q_1} - f_c\right)\dfrac{f - f_c}{f_R - f_c} & \text{if } f > f_c \end{cases} \tag{2.5}$$

and f_R is the fracture porosity. It may be helpful to assign a rupture limit for f^* using the kinetic parameter q_1, such that $f^* = 1/q_1$ sets a criterion for rupture.

According to (Rakin et al. 2004), the porosity evolution $\dot{f}$ evolves according to two phenomena within the GTN model: the growth of existing voids and the nucleation of new voids under the subjected loading. The expression for the porosity evolution may thus be defined into an additive manner such that

$$\dot{f} = \dot{f}_{nucleation} + \dot{f}_{growth} \tag{2.6}$$

where $\dot{f}_{nucleation} = A_n \dot{\varepsilon}^p_{eq}$ and $\dot{f}_{growth} = (1\text{-}f)\,\dot{\varepsilon}^p_H$ where $\dot{\varepsilon}^p_H$ is the hydrostatic component of the plastic strain rate, and A_n is a strain-rate dependent nucleation rate and other factors such as stress (Tvergaard 1989). A_n may take the Gaussian function form below as proposed by (Chu and Needleman 1980)

$$A_n = \frac{f_N}{s_N\sqrt{2\pi}}\exp\left(-\frac{1}{2}\left(\frac{p-\varepsilon_n}{s_N}\right)^2\right) \tag{2.7}$$

where f_N is a material parameter, ε_n is the strain at which half of the inclusions are broken, and s_N is the standard deviation for the nucleation strain.

The Gurson model has been further modified to account for different features such as void shape effects (Gologanu et al., 1993) and plastic anisotropy by (Benzerga and Besson 2001) where the latter authors employ the (Hill 1950) criterion. It is noteworthy that the GTN model exhibits adequate description of tensile fracture characterized by the stress triaxiality, but it fails to predict shear fracture as claimed by (Bai and Wierzbicki 2010). This brings up the discussion in the next section on the Mohr-Coulomb criterion which promises adjustment for this anomaly. Elaborate discussions on the GTN model are beyond the scope of this thesis. For a more detailed study on micromechanical modeling, the reader may refer to (Besson 2010) for a thorough review.

2.2 Mohr-Coulomb Criterion

A mathematical approach to ductile fracture modeling is the Mohr-Coulomb fracture criterion which has been widely implemented in literature, especially for the modeling of rocks and geological materials. While the criterion suits the definition of a yield criterion, it may be considered as a fracture criterion upon modification and extension. The Mohr–Coulomb (M-C) theory stems from a criterion of microcrack growth in a non-porous matrix and is one case of the widened Sandia GeoModel that unifies multiple mechanisms during deformation and failure (Fossum and Brannon 2006). The criterion has been shown to be capable of characterizing fracture of ductile metals (Bai and Wierzbicki 2008; Xue 2007). It does also depend on stress triaxiality (first invariant of the stress tensor) similar to the previously discussed micromechanical models. However, this criterion has a unique dependence on a Lode angle (parameter) that derives from the third invariant of the stress tensor, which is uncommon of the other ductile fracture criteria. In general, the M-C criterion may be understood as an extension of the maximum shear stress criterion, and it is thus poised for the prediction of shear fracture. On another note, it is important, to state that the maximum shear stress criterion does not depend on the hydrostatic stress, unlike the M-C criterion, an advantage as considered by the authors in (Bai and Wierzbicki 2010).

Bai and Wierzbicki evaluate the criterion’s applicability to ductile fracture modeling of uncracked bodies. In their work, the M-C mathematical framework is initially presented in stress space and is then transformed to strain space in order to increase the resolution of ductile fracture prediction. The authors demonstrate the effects of eight of the parameters that they propose for the fracture locus in their model. Their formulation yields a practical form of the fracture locus which is proposed for use in application by the authors. A damage evolution rule is incorporated in their model which they consider as integral to the fracture prediction technique; a linear relationship is assumed between the damage variable and equivalent plastic strain for a monotonic loading. The authors (Bai and Wierzbicki 2010) highlight how the proposed criterion is capable of predicting the material's crack path and direction. More critically, the reader must note that the M-C criterion is not capable of capturing the fracture locus of an anisotropic material and is only suitable for an isotropic material, which is a major limitation to be noted when considering the purpose of this thesis study. The general constitutive equation of the strain-based fracture locus is presented below

$$\bar{\varepsilon}_f = \left\{ \begin{array}{l} \dfrac{A}{c_2}\left[1 - c_\eta\left(\eta - \eta_0\right)\right] \times \left[c_\theta^s + \dfrac{\sqrt{3}}{2-\sqrt{3}}\left(c_\theta^{ax} - c_\theta^s\right)\left(\sec\left(\dfrac{\bar{\theta}\pi}{6}\right) - 1\right)\right] \\ \times \left[\sqrt{\dfrac{1+c_1^2}{3}}\cos\left(\dfrac{\bar{\theta}\pi}{6}\right) + c_1\left(\eta + \dfrac{1}{3}\sin\left(\dfrac{\bar{\theta}\pi}{6}\right)\right)\right] \end{array} \right\}^{-\frac{1}{n}} \tag{2.8}$$

where A, n, c_η, η_0, c_θ^s, c_θ^c, c_1 and c_2 are parameters to be determined. For a von Mises yielding function, the criterion may be reduced to the following equation

$$\bar{\varepsilon}_f = \left\{ \frac{A}{c_2}\left[\sqrt{\frac{1+c_1^2}{3}}\cos\left(\frac{\bar{\theta}\pi}{6}\right) + c_1\left(\eta + \frac{1}{3}\sin\left(\frac{\bar{\theta}\pi}{6}\right)\right)\right]\right\}^{-\frac{1}{n}} \tag{2.9}$$

As mentioned before, the incorporated damage rule assumes a linear relationship between the damage variable D and the equivalent plastic strain $\bar{\varepsilon}_p$, such that

$$D\left(\bar{\varepsilon}_p\right) = \int_0^{\bar{\varepsilon}_p} \frac{d\bar{\varepsilon}_p}{f\left(\eta, \bar{\theta}\right)} \tag{2.10}$$

where $\overline{\varepsilon}_p = \overline{\varepsilon}_f$, then $D(\overline{\varepsilon}_f) = D_c$ where D_c is a critical damage factor and is assumed to be unity.

2.3 Macromechanical Modeling – Continuum Damage Mechanics

2.3.1 Phenomenological Aspects

Material damage is often understood as the degradation of mechanical properties. Experimentally, this degradation is observed to be induced by micro-cracks, micro-voids and cavities (Murakami 1987). Continuum damage mechanics (CDM) provides a phenomenological approach to average the influence of microdefects and ignore microstructure details with the use of macroscale variables (Chow, Liu, and Asundi 1993).

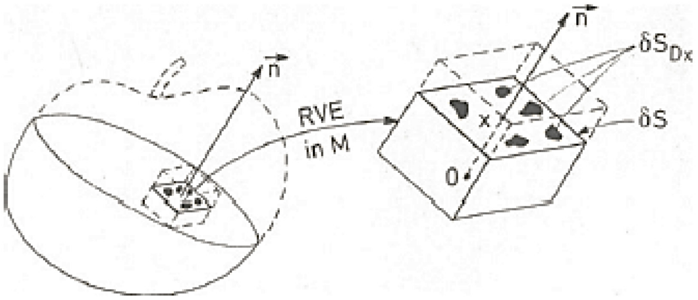

Fig. 2.1 – A Geometrical Definition of Damage (adapted from Lemaitre 1992 - A Course on Damage Mechanics)

The CDM theory was initiated with the work of (Kachanov 1958) in the study of creep rupture of metallic specimens under uniaxial tensile deformation. Kachanov proposed the concept of a continuity factor ψ which indicates a virgin material which when equal to unity. As this factor decreases down to zero, the material loses its load bearing capability. In 1969, (Rabotnov 1969) introduced a damage factor which is the complement to this continuity factor; This has further attracted researchers to the concept of damage. From Fig. 2.1, we may define the damage variable as the ratio of the area intersecting all microcracks to the area of a representative volume element of the material. We may thus express the damage variable for the uniaxial case as

$$D = \frac{S_D}{S_{RVE}} \tag{2.11}$$

where $0 \le D \le 1$. When the RVE is loaded by a unidirectional force F, we may obtain the stress in the material according to classical mechanics such that

$$\sigma = \frac{F}{S} \tag{2.12}$$

As the material sustains damage (i.e. S_D increases), the material loses portions of its surface which effectively resist the applied load. Hence, it becomes useful to introduce the concept of effective stress $\overline{\sigma}$ which may be expressed as

$$\overline{\sigma} = \frac{\sigma}{S - S_D} \tag{2.13}$$

With mathematical simplification, equation (2.13) may be re-written such that

$$\overline{\sigma} = \frac{F}{S\left(1 - \frac{S_D}{S}\right)} \tag{2.14}$$

from which we deduce

$$\overline{\sigma} = \sigma\left(\frac{1}{1 - D}\right) \tag{2.15}$$

It is noteworthy that when the damage zero, the effective stress reduces to the observed stress where $\overline{\sigma} = \sigma$. Further on this realization, the concept of strain equivalence was introduced by Rabotnov which enables visualizing the effect of damage accumulation on material stiffness. A relation between the stiffness and the damage variable may be defined below for the uniaxial case such that

$$\tilde{E} = E(1 - D) \tag{2.16}$$

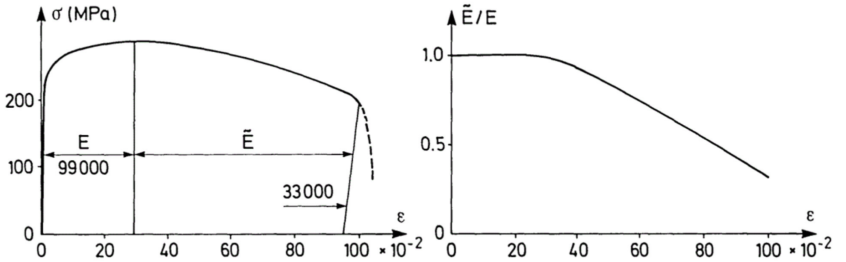

Fig. 2.2 – Degradation of Copper Stiffness
(adapted from Lemaitre 1992 after Dufailly 1975 – A Course on Damage Mechanics)

From Fig. 2.2, it becomes clear how accounting for damage enables the modeling of the post-necking region (plastic softening) in a loaded material.

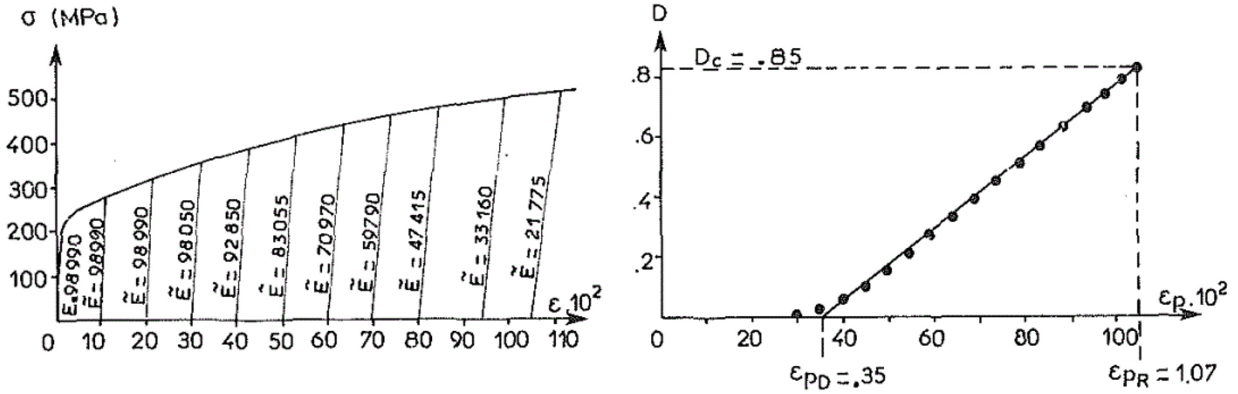

Fig. 2.3 – Ductile Damage Measurement for Copper at Room Temperature
(adapted from Lemaitre 1992– A Course on Damage Mechanics)

From Fig. 2.3, it is shown how the modus of elasticity drastically reduces, indicating the diminished load bearing capability of the damage material.

2.3.2 CDM Theory Advances

Continuum damage mechanics (CDM) is understood as a phenomenological approach to average the influence of microdefects and ignore microstructural details with the use of macroscale variables (Chow, Liu, and Asundi 1993). Kachanov pioneered the introduction of a damage variable to track material property changes in creep applications (Kachanov, 1958). Damage is incorporated in a framework of thermodynamics and takes the form of an internal variable (Coleman and Gurtin, 1967). Originally, Kachanov provided an attempt to quantify the effect of damage by proposing a scalar continuity variable ψ ranging from unity for a defect free material to zero for a failed material. The variable was assumed to be direction and orientation independent. Rabotnov later quantified the actual damage to be the ratio of the material's damaged surface to the total surface and defined it as the complement to the continuity variable ($D = 1- \psi$) to explain the loss of the material's load bearing capability (Rabotnov, 1969). Based on this definition, Rabotnov and Kachanov used the concept of effective stress, to link the damaged material configuration to a fictitious configuration, where the material is virtually assumed to be free of microdefects. The use of this concept was soon reiterated in the works of Lemaitre, Chaboche and Sidoroff (Lemaitre, 1971; Lemaitre and Chaboche, 1978; Sidoroff, 1980). Chaboche used this aspect to quantify isotropic damage using a scalar measured by the change in stiffness, strength, and toughness of the material (Chaboche, 1988). Soon after, the need for a tensorial damage framework was experimentally confirmed so that the innate material anisotropy can be captured under different stress states (Hao, Ke, and June 1985; Chow and Wang 1987; Leckie and Hayhurst 1977). With the advancements in the theory, and for anisotropic damage, the damage variable took a tensorial form with the works of Murakami and Ohno (Murakami and Ohno 1981). Leckie et al. backed the account for anisotropy to accommodate non-proportional loadings (Leckie and Onat, 1981). Later, Cordebois and Sidoroff reported on the consequences of damage in an arbitrary space where the authors pioneered the extension of the effective stress tensor in the anisotropic damage formulation (J. P. Cordebois and Sidoroff, 1982). This was done with the introduction of a fourth order damage effect tensor, a tensorial linear operator commonly known as M(D) and is used to link the damaged configuration of the material to its fictitiously undamaged configuration. Hence, tensorial characteristics were assumed for the internal damage variable (Sidoroff, 1980). For simpler use and applicability, the damage variable is derived as second order tensor using its principal directions. While propositions for a fourth rank damage tensor were done by Onat and Leckie (Onat and Leckie, 1988), the use of a second order damage tensor was adequately justified with the work of Sidoroff who presented a study on its use and admitted some limitations, but still deemed it as widely applicable (Sidoroff, 1980). Leckie and Onat later acknowledged the general use of a second order tensor (Leckie and Onat, 1981; Onat and Leckie, 1988). Based on those formulations and building on the works of Cordebois and Sidoroff (J. P. Cordebois and Sidoroff, 1982), Hao et al. proposed an anisotropic ductile damage model, and a criterion of deformation instability (Hao et al., 1985); the model was used for the predicting forming limits curves (FLC). A noteworthy formulation done by Hao et al. is extending the concept of strain hardening in plasticity to strengthening in damage. Coupling anisotropic damage with the plasticity is achieved by replacing the nominal stress with its effective value in the plastic potential function to refer to the fictitious configuration. Similar to the plasticity formulation, a criterion is assumed for damage accumulation. Hao et al. realize that the value of the damage strain energy release rate increases with the increase of the associated damage variables (Hao et al., 1985). Building on this realization, a scalar description of the overall damage accumulation is coupled with the damage potential to account for strengthening. This was developed by Chow et al. who presented an approach for the prediction of forming limit diagrams under non-proportional loading (Chow et al., 1997; Chow and Lu, 1989; Chow and Wang, 1987a). It is noteworthy that the previously described continuum damage mechanics formulations are time independent, and in this work, time dependency will be accounted for.

2.4 References

Bai, Yuanli, and Tomasz Wierzbicki. 2008. “A New Model of Metal Plasticity and Fracture with Pressure and Lode Dependence.” *International Journal of Plasticity* 24 (6): 1071–96. https://doi.org/10.1016/j.ijplas.2007.09.004.

Bai, Yuanli, and Tomasz Wierzbicki. 2010. “Application of Extended Mohr-Coulomb Criterion to Ductile Fracture.” *International Journal of Fracture* 161 (1): 1–20. https://doi.org/10.1007/s10704-009-9422-8.

Bauvineau L, Burlet H, Eripret C, Pineau A. 1996. “Modelling Ductile Stable Growth in a C-Mn Steel with Local Approaches.” *Pineau A, Rousselier G, Editors. Proceedings of the Euromech-Mecamat Conference on Local Approach to Fracture 86-96. Fontainebleau-France;*, 22.

Benzerga, Ahmed Amine, and Jacques Besson. 2001. “Plastic Potentials for Anisotropic Porous Solids.” *European Journal of Mechanics, A/Solids* 20 (3): 397–434. https://doi.org/10.1016/S0997-7538(01)01147-0.

Besson, J. 2010. “Continuum Models of Ductile Fracture: A Review.” *International Journal of Damage Mechanics*. https://doi.org/10.1177/1056789509103482.

Budiansky, B., J.W. Hutchinson and S. Slutsky. 1982. “Void Growth and Collapse in Viscous Solids, In:” *H.G. Hopkins and M.J. Sewell, Eds., Mechanics of Solids* The Rodney.

Chaboche, J. L. 1988. “Continuum Damage Mechanics: Part I—General Concepts.” *Journal of Applied Mechanics* 55 (March): 59–64. https://doi.org/10.1115/1.3173661.

Chow, C. L., Y. J. Liu, and A. Asundi. 1993. “An Incremental Stress-Based Constitutive Modeling on Anisotropic Damaged Materials.” *International Journal of Fracture* 64 (4): 299–319. https://doi.org/10.1007/BF00017847.

Chow, C. L., and T. J. Lu. 1989. “On Evolution Laws of Anisotropic Damage.” *Engineering Fracture Mechanics* 34 (3): 679–701. https://doi.org/10.1016/0013-7944(89)90130-6.

Chow, C. L., and June Wang. 1987. “An Anisotropic Theory of Continuum Damage Mechanics for Ductile Fracture.” *Engineering Fracture Mechanics* 27 (5): 547–58. https://doi.org/10.1016/0013-7944(87)90108-1.

Chow, C. L., L. G. Yu, and M. Y. Demeri. 1997. “A Unified Damage Approach for Predicting Forming Limit Diagrams.” *Journal of Engineering Materials and Technology* 119 (4).

American Society of Mechanical Engineers: 346. https://doi.org/10.1115/1.2812269.

Chu, C. C., and A. Needleman. 1980. “Void Nucleation Effects in Biaxially Stretched Sheets.” *Journal of Engineering Materials and Technology* 102 (3). American Society of Mechanical Engineers: 249. https://doi.org/10.1115/1.3224807.

Coleman, Bernard D., and Morton E. Gurtin. 1967. “Thermodynamics with Internal State Variables.” *The Journal of Chemical Physics* 47 (2): 597–613. https://doi.org/10.1063/1.1711937.

Cordebois, J. P., and F. Sidoroff. 1982. “Damage Induced Elastic Anisotropy.” In *Mechanical Behavior of Anisotropic Solids / Comportment Méchanique Des Solides Anisotropes*, 761–74. Dordrecht: Springer Netherlands. https://doi.org/10.1007/978-94-009-6827-1_44.

Fossum, A. F., and R. M. Brannon. 2006. “On a Viscoplastic Model for Rocks with Mechanism-Dependent Characteristic Times.” *Acta Geotechnica* 1 (2): 89–106. https://doi.org/10.1007/s11440-006-0010-z.

Gologanu, Mihai, Jean Baptiste Leblond, and Josette Devaux. 1993. “Approximate Models for Ductile Metals Containing Non-Spherical Voids-Case of Axisymmetric Prolate Ellipsoidal Cavities.” *Journal of the Mechanics and Physics of Solids* 41 (11): 1723–54. https://doi.org/10.1016/0022-5096(93)90029-F.

Gurson, A. L. 1977. “Continuum Theory of Ductile Rupture by Void Nucleation and Growth: Part I—Yield Criteria and Flow Rules for Porous Ductile Media.” *Journal of Engineering Materials and Technology* 99 (1): 2. https://doi.org/10.1115/1.3443401.

Hao, Lee, Peng Ke, and Wang June. 1985. “An Anisotropic Damage Criterion for Deformation Instability and Its Application to Forming Limit Analysis of Metal Plates.” *Engineering Fracture Mechanics* 21 (5): 1031–54. https://doi.org/10.1016/0013-7944(85)90008-6.

Hill, R. 1950. *The Mathematical Theory of Plasticity. Oxford University Press Ic., New York.* https://doi.org/10.1002/9780470694626.ch6.

Kachanov, Lo M. 1958. “On the Creep Fracture Time.” *Izv Akad, Nauk USSR Otd Tech 8*, 26–31.

Leckie, F.A., and D.R. Hayhurst. 1977. “Constitutive Equations for Creep Rupture.” *Acta Metallurgica* 25 (9): 1059–70. https://doi.org/10.1016/0001-6160(77)90135-3.

Leckie, F. A., and E. T. Onat. 1981. “Tensorial Nature of Damage Measuring Internal Variables.” In *Physical Non-Linearities in Structural Analysis*, 140–55. Berlin, Heidelberg: Springer Berlin Heidelberg. https://doi.org/10.1007/978-3-642-81582-9_20.

Lemaitre, J. 1971. “Evolution of Dissipation and Damage in Metals Subject to Dynamic Loading.” *Proc ICM-1-Kyoto, Japan.*

Lemaitre, J., and J. L. Chaboche. 1978. “Aspects Phénoménologiques de La Rupture Par Endommagement.” *Journal de Mécanique Appliquée* 2 (3): 317–65. http://trid.trb.org/view.aspx?id=1048150.

Marino, B., F. Mudry, and A. Pineau. 1985. “Experimental Study of Cavity Growth in Ductile

Rupture.” *Engineering Fracture Mechanics* 22 (6): 989–96. https://doi.org/10.1016/0013-7944(85)90038-4.

McClintock, F A. 1968. “A Criterion for Ductile Fracture by the Growth of Holes.” *Journal of Applied Mechanics* 35 (2): 363–71. https://doi.org/10.1115/1.3601204.

Miller, Timothy C., and Ted L. Anderson. 1995. “Void Growth Model Relating Fracture Toughness and Constraint.” In *ASTM Special Technical Publication*, 87–107.

Murakami, S., and N. Ohno. 1981. “A Continuum Theory of Creep and Creep Damage.” In *Creep in Structures*, 422–44. Berlin, Heidelberg: Springer Berlin Heidelberg. https://doi.org/10.1007/978-3-642-81598-0_28.

Murakami, Sumio. 1987. “Anisotropic Aspects of Material Damage and Application of Continuum Damage Mechanics.” In *Continuum Damage Mechanics Theory and Application*, 91–133. Vienna: Springer Vienna. https://doi.org/10.1007/978-3-7091-2806-0_3.

Onat, E, and F Leckie. 1988. “Representation of Mechanical Behavior in the Presence of Changing Internal Structure.” *Applied Mechanics* 55 (1): 10. https://doi.org/10.1115/1.3173630.

Rabotnov, YN. 1969. “Creep Problems in Structural Members.” http://cds.cern.ch/record/103309.

Rakin, M., Z. Cvijovic, V. Grabulov, S. Putic, and A. Sedmak. 2004. “Prediction of Ductile Fracture Initiation Using Micromechanical Analysis.” *Engineering Fracture Mechanics* 71 (4–6): 813–27. https://doi.org/10.1016/S0013-7944(03)00013-4.

Rice, J.R., and D.M. Tracey. 1969. “On the Ductile Enlargement of Voids in Triaxial Stress Fields∗.” *Journal of the Mechanics and Physics of Solids* 17 (3): 201–17. https://doi.org/10.1016/0022-5096(69)90033-7.

Sidoroff, F. 1980. “Description of Anisotropic Damage Applications to Elasticity.” *Physical Non-Linearities in Structural Analysis, IUTAM Series*, 237–44.

Tvergaard, V, and A Needleman. 1984. “Analysis of the Cup-Cone Round Tensile Fracture.” *Acta Metallurgica* 32 (1): 157–69. https://doi.org/10.1016/0001-6160(84)90213-X.

Tvergaard, Viggo. 1989. “Material Failure by Void Growth to Coalescence.” *Advances in Applied Mechanics* 27 (C): 83–151. https://doi.org/10.1016/S0065-2156(08)70195-9.

Xue, Liang, and Tomasz Wierzbicki. 2007. “Ductile Fracture Modeling-Theory, Experimental Investigation and Numerical Verification.” *Department of Mechanical Engineering*.

CHAPTER 3
CONSTITUTIVE MODELING AND NUMERICAL METHOD

In this chapter, the aim is to derive a constitutive model able to reproduce the viscoplastic response of a ductile material up until the point of failure. In what follows, the model is developed in the framework of finite strains.

3.1 Kinematics

In this work, the model is defined for finite strains. The position of the material point in the new configuration may be defined as $\mathbf{x} = \chi(\mathbf{X}, t)$ where $\mathbf{X}$ is the referential non-deformed material position. The deformation gradient $\mathbf{F}$ can be decomposed in a multiplicative manner into elastic $\mathbf{F}^e$ and plastic $\mathbf{F}^p$ parts where $\mathbf{F} = \mathbf{F}^e\mathbf{F}^p$. The velocity gradient $\mathbf{L}$ is expressed as the product between the time derivative of the deformation gradient and the inverse of deformation gradient such that $\mathbf{L} = \dot{\mathbf{F}}\mathbf{F}^{-1}$. The velocity gradient $\mathbf{L}$ can be expressed in function of a spin component $\mathbf{W}$ (skew-symmetric part) and a rate of total deformation $\mathbf{D}$ (symmetric part) as $\mathbf{L} = \mathbf{D} + \mathbf{W}$. Furthermore, the velocity gradient $\mathbf{L}$ can be decomposed additively into elastic $\mathbf{L}^e$ and plastic $\mathbf{L}^p$ such that $\mathbf{L} = \mathbf{L}^e + \mathbf{L}^p$. The plastic part of the velocity gradient can be decomposed into symmetric $\mathbf{D}^p$ and skew-symmetric $\mathbf{W}^p$ parts where $\mathbf{L}^p = \mathbf{D}^p + \mathbf{W}^p$. Similarly, the elastic part of the velocity gradient can be decomposed into symmetric $\mathbf{D}^e$ and askew-symmetric $\mathbf{W}^e$ parts where $\mathbf{L}^e = \mathbf{D}^e + \mathbf{W}^e$. Finally, for finite deformation, the total rate of deformation can be additively decomposed into elastic and plastic parts as suggested by (Khan and Huang, 1995) as

$\mathbf{D} = \mathbf{D}^e + \mathbf{D}^p$. In the next chapter, we validate the applicability of the model for the case of uniaxial tensile deformation. Assuming that the material exhibits isochoric deformation properties, then the volume map (Jacobian) of the deformation gradient must be equal to unity. The components of the deformation gradient $\mathbf{F}$ can be found by setting the determinant of the Jacobian equal to unity such that $J = \det \mathbf{F} = \lambda_1 \lambda_2 \lambda_3 = 1$. For a uniaxial loading, we assume $\lambda_2 = \lambda_3$ which yields $\lambda_2 = \lambda_3 = \lambda_1^{-1/2}$ from which the diagonal elements of the deformation gradient can be calculated.

3.2 Constitutive Equations of the Damage Coupled Plastic Model

The formulations of the anisotropic CDM model follow a thermodynamics framework of positive dissipation. The unified damage approach of Chow et al. provides a time independent framework (Chow et al., 1997). In this section, we propose a time dependent framework that directly incorporates the viscosity effect in both the plasticity and the damage formulations. The time dependent framework will allow capturing the strain-rate sensitivity of ductile alloys at elevated temperatures.

3.2.1 Damage Coupled Elasticity

The elastic energy equivalence hypothesis (Cordebois and Sidoroff 1982) provide the basis for the development. We may define the damage variable for an isotropic case as

$$D = \frac{A - \tilde{A}}{A} \tag{3.1}$$

where D is a scalar damage variable, A is the material's total area and $\tilde{A}$ is the material's area excluding microdefects. The effective stress may be defined as

$$\tilde{S} = \frac{F}{\tilde{A}} = \frac{F}{A(1-D)} = \frac{S}{(1-D)} \tag{3.2}$$

For the anisotropic case, one may deduce the expression of the effective stress tensor for anisotropic damage (Cordebois and Sidoroff 1982), such that

$$\tilde{S}_{ij} = M_{ijkl} S_{kl} \tag{3.3}$$

where M_{ijkl} is the fourth order damage effect tensor, a linear operator that links the damaged material configuration to its fictitious undamaged configuration. For this case, the damage tensor is of second order D_{ij} , and the damage effect tensor may be expressed using the principal components of the damage tensor such that:

$$M_{ijkl} = \begin{bmatrix} \frac{1}{1-D_1} & 0 & 0 & 0 & 0 & 0 \\ 0 & \frac{1}{1-D_2} & 0 & 0 & 0 & 0 \\ 0 & 0 & \frac{1}{1-D_3} & 0 & 0 & 0 \\ 0 & 0 & 0 & \frac{1}{\sqrt{(1-D_2)(1-D_3)}} & 0 & 0 \\ 0 & 0 & 0 & 0 & \frac{1}{\sqrt{(1-D_3)(1-D_1)}} & 0 \\ 0 & 0 & 0 & 0 & 0 & \frac{1}{\sqrt{(1-D_1)(1-D_2)}} \end{bmatrix} \tag{3.4}$$

For a representative volume element (RVE) under applied stress, the elastic energy is defined as

$$W^e(S) = \tfrac{1}{2} S_{ij} C^{-1}_{ijkl} S_{kl} \tag{3.5}$$

where C^{-1}_{ijkl} is the material compliance tensor.

According to the hypothesis of energy equivalence, the elastic energy of the damaged configuration can be determined by replacing the stress with the effective stress such that $W^e(S_{ij}, D_{ij} \neq 0) = W^e(\tilde{S}_{ij}, D_{ij} = 0)$, thus

$$W^e(S_{ij}, D_{ij}) = \tfrac{1}{2} \tilde{S}_{ij} C^{-1}_{ijkl} \tilde{S}_{kl} = \tfrac{1}{2} S_{ij} M_{jikl} C^{-1}_{klmn} M_{mnop} S_{op} = \tfrac{1}{2} S_{ij} \tilde{C}^{-1}_{ijkl} S_{kl} \tag{3.6}$$

which imposes a symmetry condition on the effective elasticity compliance tensor, to which we define the expression below

$$\tilde{C}^{-1}_{ijop} = M_{ijkl} C^{-1}_{klmn} M_{mnop} \tag{3.7}$$

Based on the thermodynamics of an irreversible process, we calculate the elastic energy release rate, commonly known as the associated variable for the damage tensor D_{ij}, such that

$$\begin{aligned} Y_{op} &= -\frac{\partial W^e(S,D)}{\partial D_{ij}} = -S_{ij} \left\{ C^{-1}_{ijkl} M_{klmn} \frac{\partial M_{mnop}}{\partial D_{qr}} \right\}^s S_{qr} \\ &= -S_{ij} \left\{ \tilde{C}^{-1}_{ijkl} M^{-1}_{klmn} \frac{\partial M_{mnop}}{\partial D_{qr}} \right\}^s S_{qr} \end{aligned} \tag{3.8}$$

where 's' denotes taking the symmetric part of the resulting tensor within the curly brackets. For a damage dissipative potential function Φ_d, we may propose the time rate of damage evolution, such that

$$\dot{D}_{ij} = -\frac{\partial \Phi^d}{\partial Y_{ij}} \tag{3.9}$$

Note that although the stress tensor is derived in an arbitrary coordinate space, the developed equations are expressed in function of the principal values of the damage tensor where $D_{11} = D_1$, $D_{22} = D_2$, $D_{33} = D_3$ and $D_{23} = D_{13} = D_{12} = 0$. The principal directions of the damage tensor will coincide with that of the stress tensor only in the simple cases of uniaxial loadings (Chen and Chow, 1995). For the case of general loading conditions, a rotation to the damage tensor is caused. Thus, for the damage formulations to hold, a coordinate transformation of the associated variable for damage Y_{ij} is necessary. This can be achieved with the root-finding of a third order characteristic polynomial for Y_{ij} which allows the determination of its Eigen values. The characteristic polynomial can be obtained by equating the determinant of Y_{ij} to zero. The resultant third order polynomial is solved by trigonometric approximation using the method of (Kronenburg 2013) for a 3x3 matrix, the case when Y_{ij} is expressed in matricial form.

3.2.2 Damage Coupled Plasticity

The development of the constitutive equations of visco-plasticity coupled with damage is achieved by using the effective stress tensor instead of the stress tensor for the plastic potential of undamaged material (Chow et al., 1997). A damage coupled plastic potential is used to express the yield criterion f^p which incorporates the equivalent plastic stress according to Hill (1948) criterion that describes anisotropic material plasticity of metals, such that:

$$f^p = \tilde{S}^{eq} - R\left(p\right) = 0 \tag{3.10}$$

where $\tilde{S}_{eq}$ is the effective equivalent plastic stress and $R(p)$ is an isotropic hardening term. We define the effective Hill equivalent plastic stress as

$$\tilde{S}^{eq} = \left(\tfrac{1}{2}\tilde{S}_{ij}H_{ijkl}\tilde{S}_{kl}\right)^{1/2} \qquad (3.11$$

and the fourth order Hill tensor may be written in matricial form as

$$H_{ijkl} = \begin{bmatrix} G+H & -H & -G & 0 & 0 & 0 \\ -H & H+F & -F & 0 & 0 & 0 \\ -G & -F & F+G & 0 & 0 & 0 \\ 0 & 0 & 0 & 2L & 0 & 0 \\ 0 & 0 & 0 & 0 & 2M & 0 \\ 0 & 0 & 0 & 0 & 0 & 2N \end{bmatrix} \tag{3.12}$$

where F, G, H, L, M and N are material constants which can be determined experimentally according to Hill 1948.

The effective stress tensor $\tilde{S}_{ij}$ is expressed in terms of the stress tensor as suggested in equation (3.3). S_{ij} is integrated from the following stress rate expression

$$\dot{S}_{ij} = \tilde{C}_{ijop}\left[D_{op} - D^{P}_{op}\right] \tag{3.13}$$

where

$$\tilde{C}_{ijop} = M^{-1}_{ijkl} C_{klmn} M^{-1}_{mnop} \tag{3.14}$$

The plastic rate of deformation tensor D^{P}_{ij} can be derived from the classical theory of plasticity, such that:

$$D^{P}_{ij} = \lambda^{p} \frac{\partial F^{p}}{\partial S_{ij}} = \frac{\lambda^{p}}{2\tilde{S}^{eq}} H_{ijkl} \tilde{S}_{kl} \tag{3.15}$$

where the plastic multiplier λ^{p} is approximated by the cumulative plastic strain rate $\dot{p}$. The cumulative plastic strain rate $\dot{p}$ is quantified using a visco-plastic strain-sensitive power law, such that

$$\dot{p} = \gamma^{p} \left(\frac{\tilde{S}^{eq}}{s} \right)^{1/m} \tag{3.16}$$

where γ^{p} is an initial plastic rate, m is a material rate sensitive parameter, and s is a shear strength resistance which evolves according to the power law proposed by (Stringfellow, Parks, and Olson 1992) such that

$$\dot{s} = \frac{s}{n^h}\left(\frac{s^s}{s}\right)^{n^h} \tag{3.17}$$

where n^h is a fitted hardening coefficient and s^s is a hardening saturation limit. Note that s^0 is the strength resistance is at the onset of plasticity, the initial value for s.

3.2.3 Damage Evolution

In analogy to the plastic yield surface, the concept of a damage surface is proposed (Chow and Wang, 1987a, 1987b). To model the evolution of anisotropic damage, a plastic damage criterion is proposed using a damage potential f^d as follows

$$f^d = Y^{eq} - Z(q) = 0 \tag{3.18}$$

where Y^{eq} is the equivalent elastic energy release rate and $Z(q)$ is a damage strengthening term, which accounts for the overall accumulation of damage in the material element. From equation (3.9), the damage evolution $\dot{D}^d_{ij}$ may be evaluated by assuming the dissipative damage potential f^d such that

$$\dot{D}^d_{ij} = -\lambda^d \frac{\partial f^d}{\partial Y_{kl}} = -\frac{\lambda^d}{2Y^{eq}} L^d_{ijkl} Y_{kl} \tag{3.19}$$

where λ^d is the Lagrange multiplier that can be approximated by the cumulative plastic damage rate $\dot{q}$. Equation (3.21) expresses the rate for damage accumulation, which allows the quantification of the damage at any deformation level. In general, a critical damage value, less then unity, is associated with material failure. The reader is referred to the works of Lemaitre et al. for material specific critical rupture limits (Lemaitre, 1985; Lemaitre et al., 2000). L^d_{ijkl} is the fourth order plastic damage characteristic tensor in its matricial form as

$$L^d_{ijkl} = \begin{bmatrix} 1 & \eta & \eta & 0 & 0 & 0 \\ \eta & 1 & \eta & 0 & 0 & 0 \\ \eta & \eta & 1 & 0 & 0 & 0 \\ 0 & 0 & 0 & \frac{1}{2}(1-\eta) & 0 & 0 \\ 0 & 0 & 0 & 0 & \frac{1}{2}(1-\eta) & 0 \\ 0 & 0 & 0 & 0 & 0 & \frac{1}{2}(1-\eta) \end{bmatrix} \tag{3.20}$$

where η is an experimentally determined material constant.

The cumulative plastic damage rate is quantifies using a strain rate sensitive damage power law as

$$\dot{q} = \gamma^d \left(\frac{Y^{eq}}{Y^0} \right)^{1/n} \tag{3.21}$$

where γ^d is the initial damage rate, n is a rate sensitive parameter and Y^0 is the damage strengthening resistance (assumed constant). We define the effective equivalent energy release rate below as

$$Y^{eq} = \left(\tfrac{1}{2} Y_{ij} L^d_{ijkl} Y_{kl} \right)^{1/2} \tag{3.22}$$

3.3 Time Integration Method

In this section, an implicit integration algorithm is proposed to integrate the constitutive relations presented in section 2. This section summarized the main features of the numerical implementation. To achieve higher computational efficiency there is a need to ensure adequate and timely convergence properties for the stress and damage tensorial components.

For the symmetric stress tensor, six Voigt components are identified such that

$$[S]^T = [S_{11} \quad S_{22} \quad S_{33} \quad S_{23} \quad S_{13} \quad S_{12}] \tag{3.23}$$

As a second order tensor, the damage components can be identified similarly

$$[D]^T = [D_{11} \quad D_{22} \quad D_{33} \quad D_{23} \quad D_{13} \quad D_{12}] \tag{3.24}$$

However, in the development of the constitutive model, the damage rate is formulated in its principal direction, where only the principal values for the damage tensor D_{11}, D_{22} and D_{33} are of non-zero value. Then, the damage components may be expressed in the following vector

$$[D]^T = [D_{11} \quad D_{22} \quad D_{33}] \tag{3.25}$$

Generally, for a proportional loading, the shearing components S_{23}, S_{13} and S_{12} are zero, which vanish the non-diagonal components Y_{23}, Y_{13}, and Y_{12} of the damage energy release rate. In the case when changes to the loading conditions exist, there will be non-proportionality in the loading. This implies that the associated damage variable Y_{ij} will have non-zero components across the directions 23, 13 and 12. Thus, the principal values of Y_{ij} are obtained, so that the coincidence of the stress and damage coordinate systems is guaranteed. Combining all 6 stresses and 3 damage components, the variables may be represented in the vector below

$$[X]^T = [S_{11} \quad S_{22} \quad S_{33} \quad S_{23} \quad S_{13} \quad S_{12} \quad D_{11} \quad D_{22} \quad D_{33}] \tag{3.26}$$

Those variables are described by the differential equations given in equations (3.12) and (3.19). An implicit time integration method following the backward Euler scheme is used to solve the system of nonlinear equations. For example, the first component of the stress tensor S_{11}^{t+1} at the current time step $t+1$ is approximated such that

$$S_{11}^{t+1} = S_{11}^{t} + \dot{S}_{11}^{t+1}\Delta t \tag{3.27}$$

With t being the previous time step and Δt is the time increment. It is sought to minimize the difference (the residual) between the rate of the stress component and its previous and current increment over the time step. Following this analysis, a residual function $R_{S_{11}}$ for the variable S_{11} is defined and is minimized by the Newton-Raphson procedure. The residual $R_{S_{11}}$ may be expressed below as

$$R_{S_{11}}^{t+1} = \frac{S_{11}^{t+1} - S_{11}^{t}}{\Delta t} - \dot{S}_{11}^{t+1} \tag{3.28}$$

Similarly, for the remaining stress and damage residuals, we express the functions below

$$\begin{gathered} R_{S_{22}}^{t+1} = \frac{S_{22}^{t+1} - S_{22}^{t}}{\Delta t} - \dot{S}_{22}^{t+1} \\ \times \\ R_{D_{33}}^{t+1} = \frac{D_{33}^{t+1} - D_{33}^{t}}{\Delta t} - \dot{D}_{33}^{t+1} \end{gathered} \tag{3.29}$$

The rate equations for each of the variables are provided in the Appendix. The calculated residuals may be collected in the residual vector below such that

$$[R]^T = \begin{bmatrix} R_{S_{11}} & R_{S_{22}} & R_{S_{33}} & R_{S_{23}} & R_{S_{13}} & R_{S_{12}} & R_{D_{11}} & R_{D_{22}} & R_{D_{33}} \end{bmatrix} \tag{3.30}$$

The state variables at the end of the increment are referred to by $[X]_{9x1}^{t+1}$ while the variables at the beginning of the increment by $[X]_{9x1}^{t}$. The Newton-Raphson procedure is used for the constitutive updating as follows

$$[X]_{9x1}^{t+1} = [X]_{9x1}^{t} - \mathrm{inv}\left[\underbrace{\frac{\partial[R]}{\partial[X]}}_{\text{Jacobian}}\right]^{t+1} [R]^{t+1} \tag{3.31}$$

where ‘inv’ denotes the inverse of the Jacobian matrix. In the next step, the partial derivatives of the nine residuals with respect to all nine variables need to be calculated. Those quantities are used to define the Jacobian matrix. The Jacobian may then be expressed in matricial form (9x9) as follows

$$\left[\underbrace{\frac{\partial[\mathrm{R}]}{\partial[\mathrm{X}]}}_{\text{Jacobian}}\right]^{t+1}=\begin{bmatrix}
\frac{\partial R_{S_{11}}}{\partial S_{11}} & \frac{\partial R_{S_{11}}}{\partial S_{22}} & \frac{\partial R_{S_{11}}}{\partial S_{33}} & \frac{\partial R_{S_{11}}}{\partial S_{23}} & \frac{\partial R_{S_{11}}}{\partial S_{13}} & \frac{\partial R_{S_{11}}}{\partial S_{12}} & \frac{\partial R_{S_{11}}}{\partial D_{11}} & \frac{\partial R_{S_{11}}}{\partial D_{22}} & \frac{\partial R_{S_{11}}}{\partial D_{33}} \\
\frac{\partial R_{S_{22}}}{\partial S_{11}} & \frac{\partial R_{S_{22}}}{\partial S_{22}} & \frac{\partial R_{S_{22}}}{\partial S_{33}} & \frac{\partial R_{S_{22}}}{\partial S_{23}} & \frac{\partial R_{S_{22}}}{\partial S_{13}} & \frac{\partial R_{S_{22}}}{\partial S_{12}} & \frac{\partial R_{S_{22}}}{\partial D_{11}} & \frac{\partial R_{S_{22}}}{\partial D_{22}} & \frac{\partial R_{S_{22}}}{\partial D_{33}} \\
\frac{\partial R_{S_{33}}}{\partial S_{11}} & \frac{\partial R_{S_{33}}}{\partial S_{22}} & \frac{\partial R_{S_{33}}}{\partial S_{33}} & \frac{\partial R_{S_{33}}}{\partial S_{23}} & \frac{\partial R_{S_{33}}}{\partial S_{13}} & \frac{\partial R_{S_{33}}}{\partial S_{12}} & \frac{\partial R_{S_{33}}}{\partial D_{11}} & \frac{\partial R_{S_{33}}}{\partial D_{22}} & \frac{\partial R_{S_{33}}}{\partial D_{33}} \\
\frac{\partial R_{S_{23}}}{\partial S_{11}} & \frac{\partial R_{S_{23}}}{\partial S_{22}} & \frac{\partial R_{S_{23}}}{\partial S_{33}} & \frac{\partial R_{S_{23}}}{\partial S_{23}} & \frac{\partial R_{S_{23}}}{\partial S_{13}} & \frac{\partial R_{S_{23}}}{\partial S_{12}} & \frac{\partial R_{S_{23}}}{\partial D_{11}} & \frac{\partial R_{S_{33}}}{\partial D_{22}} & \frac{\partial R_{S_{23}}}{\partial D_{33}} \\
\frac{\partial R_{S_{13}}}{\partial S_{11}} & \frac{\partial R_{S_{13}}}{\partial S_{22}} & \frac{\partial R_{S_{13}}}{\partial S_{33}} & \frac{\partial R_{S_{13}}}{\partial S_{23}} & \frac{\partial R_{S_{13}}}{\partial S_{13}} & \frac{\partial R_{S_{13}}}{\partial S_{12}} & \frac{\partial R_{S_{13}}}{\partial D_{11}} & \frac{\partial R_{S_{13}}}{\partial D_{22}} & \frac{\partial R_{S_{13}}}{\partial D_{33}} \\
\frac{\partial R_{S_{12}}}{\partial S_{11}} & \frac{\partial R_{S_{12}}}{\partial S_{22}} & \frac{\partial R_{S_{12}}}{\partial S_{33}} & \frac{\partial R_{S_{12}}}{\partial S_{23}} & \frac{\partial R_{S_{12}}}{\partial S_{13}} & \frac{\partial R_{S_{12}}}{\partial S_{12}} & \frac{\partial R_{S_{12}}}{\partial D_{11}} & \frac{\partial R_{S_{12}}}{\partial D_{22}} & \frac{\partial R_{S_{12}}}{\partial D_{33}} \\
\frac{\partial R_{D_{11}}}{\partial S_{11}} & \frac{\partial R_{D_{11}}}{\partial S_{22}} & \frac{\partial R_{D_{11}}}{\partial S_{33}} & \frac{\partial R_{D_{11}}}{\partial S_{23}} & \frac{\partial R_{D_{11}}}{\partial S_{13}} & \frac{\partial R_{D_{11}}}{\partial S_{12}} & \frac{\partial R_{D_{11}}}{\partial D_{11}} & \frac{\partial R_{D_{11}}}{\partial D_{22}} & \frac{\partial R_{D_{11}}}{\partial D_{33}} \\
\frac{\partial R_{D_{22}}}{\partial S_{11}} & \frac{\partial R_{D_{22}}}{\partial S_{22}} & \frac{\partial R_{D_{22}}}{\partial S_{33}} & \frac{\partial R_{D_{22}}}{\partial S_{23}} & \frac{\partial R_{D_{22}}}{\partial S_{13}} & \frac{\partial R_{D_{22}}}{\partial S_{12}} & \frac{\partial R_{D_{22}}}{\partial D_{11}} & \frac{\partial R_{D_{22}}}{\partial D_{22}} & \frac{\partial R_{D_{22}}}{\partial D_{33}} \\
\frac{\partial R_{D_{33}}}{\partial S_{11}} & \frac{\partial R_{D_{33}}}{\partial S_{22}} & \frac{\partial R_{D_{33}}}{\partial S_{33}} & \frac{\partial R_{D_{33}}}{\partial S_{23}} & \frac{\partial R_{D_{33}}}{\partial S_{13}} & \frac{\partial R_{D_{33}}}{\partial S_{12}} & \frac{\partial R_{D_{33}}}{\partial D_{11}} & \frac{\partial R_{D_{33}}}{\partial D_{22}} & \frac{\partial R_{D_{33}}}{\partial D_{33}}
\end{bmatrix} \tag{3.32}$$

The implementation in MATLAB® follows from the above development, and the rate equations of the model are solved using the Newton Raphson algorithm as summarized in the flowchart of Fig. 3.1.

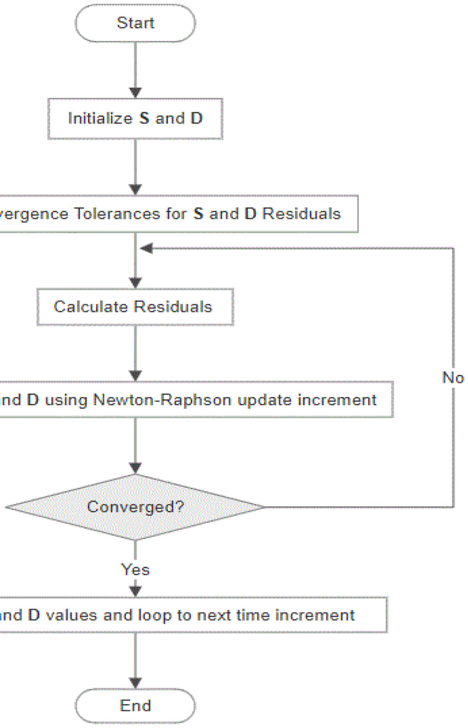

Fig. 3.1 – Flowchart of the Implicit Integration Algorithm

This concludes the development of the model and the numerical method. In the next chapter, an experimental study is presented on the behavior of TRC sheet of Mg AZ31B alloy for a multitude of strain rates and temperatures. The experimental observations will be used to assess the model's capability in capturing the plastic deformation and damaging behaviors of the alloy.

3.4 References

Chen, X. F., and C. L. Chow. 1995. “On Damage Strain Energy Release Rate Y.” *International Journal of Damage Mechanics* 4 (3): 251–63. https://doi.org/10.1177/105678959500400304.

Chow, C. L., and June Wang. 1987a. “An Anisotropic Theory of Continuum Damage Mechanics for Ductile Fracture.” *Engineering Fracture Mechanics* 27 (5): 547–58. https://doi.org/10.1016/0013-7944(87)90108-1.

Chow, C. L., and June Wang. 1987b. “An Anisotropic Theory of Elasticity for Continuum Damage Mechanics.” *International Journal of Fracture* 33 (1): 3–16. https://doi.org/10.1007/BF00034895.

Chow, C. L., L. G. Yu, and M. Y. Demeri. 1997. “A Unified Damage Approach for Predicting Forming Limit Diagrams.” *Journal of Engineering Materials and Technology* 119 (4). American Society of Mechanical Engineers: 346. https://doi.org/10.1115/1.2812269.

Cordebois, J. P., and F. Sidoroff. 1982a. “Damage Induced Elastic Anisotropy.” In *Mechanical Behavior of Anisotropic Solids / Comportment Méchanique Des Solides Anisotropes*, 761–74. Dordrecht: Springer Netherlands. https://doi.org/10.1007/978-94-009-6827-1_44.

Cordebois, J.P., and F. Sidoroff. 1982b. “Endommagement Anisotrope En Élasticité et Plasticité.” *Journal de Mécanique Théorique et Appliquée*, 45–60.

Hill, R. 1950. *The Mathematical Theory of Plasticity*. *Oxford University Press Ic., New York*. https://doi.org/10.1002/9780470694626.ch6.

Khan, Akhtar S., and Sujian. Huang. 1995. *Continuum Theory of Plasticity*. Wiley. https://books.google.com/books/about/Continuum_Theory_of_Plasticity.html?id=l1FPaaY355gC.

Kronenburg, M. J. 2013. “A Method for Fast Diagonalization of a 2x2 or 3x3 Real Symmetric Matrix,” June. http://arxiv.org/abs/1306.6291.

Lemaitre, J. 1985. “A Continuous Damage Mechanics Model for Ductile Fracture.” *J. Eng. Mater. Technol.(Trans. ASME)* 107 (January 1985): 83–89. https://doi.org/10.1115/1.3225775.

Lemaitre, Jean, Rodrigue Desmorat, and Maxime Sauzay. 2000. “Anisotropic Damage Law of Evolution.” *European Journal of Mechanics - A/Solids* 19 (2). Elsevier Masson: 187–208. https://doi.org/10.1016/S0997-7538(00)00161-3.

Stringfellow, R. G., D. M. Parks, and G. B. Olson. 1992. “A Constitutive Model for Transformation Plasticity Accompanying Strain-Induced Martensitic Transformations in Metastable Austenitic Steels.” *Acta Metallurgica Et Materialia* 40 (7): 1703–16. https://doi.org/10.1016/0956-7151(92)90114-T

CHAPTER 4
MODEL VALIDATION: APPLICATION FOR TWIN ROLL CAST MG ALLOY AZ31B

In this chapter, the anisotropic model is experimentally validated for the case of uniaxial tensile deformation. Mg AZ31B stress-strain data is obtained and utilized to assess the model's capability in capturing the material's elastic, plastic and post-necking behavior. Implementation aspects are discussed including the parameter identification process.

4.1 Experimental Investigation for TRC Mg Alloy AZ31B

Magnesium alloys are known to exhibit low formability at room temperatures due to their HCP crystal structure. Two independent basal slip systems $\{0001\}\langle 11\bar{2}0\rangle$ are found in magnesium. The homogeneous plastic deformation of a polycrystalline Mg requires the activation of additional deformation modes to satisfy the Taylor criterion (Chino et al., 2008; Koike et al., 2003). The deformation modes that can be active while loading Mg are; $\langle \mathrm{a}\rangle$ basal slip $\{0001\}\langle 11\bar{2}0\rangle$, $\langle \mathrm{a}\rangle$ prismatic slip $\{1\bar{1}00\}\langle 11\bar{2}0\rangle$, $\langle \mathrm{a}\rangle$ pyramidal slip $\{10\bar{1}1\}\langle 11\bar{2}0\rangle$, $\langle \mathrm{c}+\mathrm{a}\rangle$ pyramidal slip $\{0001\}\langle 11\bar{2}0\rangle$, contraction twin $\{10\bar{1}1\}\langle \bar{1}012\rangle$ and extension twin $\{10\bar{1}2\}\langle \bar{1}011\rangle$. At elevated temperatures, additional deformation modes such as grain boundary sliding (GBS), grain fragmentation and recrystallization can contribute to overall behavior of Mg alloys. Therefore, higher ductility can be achieved.

Experimental uniaxial tensile test data at different strain rates and temperatures on Twin Roll Cast sheets of Mg AZ31B Alloy are used for the model validation (Ayoub et al., 2018). The experimental data is used to validate the model capability in capturing the experimental strain to fracture, work of fracture, yielding and ultimate tensile. The uniaxial tensile tests were performed at four different temperatures (25 °C, 100°C, 200 °C, and 300 °C) and at three strain rates (0.001 s^{-1}, 0.01 s^{-1} and 0.1 s^{-1}). The strains were measured using a laser extensometer and the stresses were calculated by dividing the measured load by the current area. The current area was estimated by assuming that deformation occurs at constant volume. It is acknowledged that this assumption holds true up to the onset of plastic instability.

In Fig. 4.1 (a), the stress-strain curve corresponds to a representative uniaxial tensile test done at room temperature. As observed, the overall effect of strain rate appears to be non-significant. However, the effect has a higher influence on the strain to failure (ductility). As the strain rate increases, the yield stress increases up to 7%. This effect is similar on the ultimate tensile stress, as it increases up to 9%. The specimen ductility shows a minor decrease when strain rate is increased from 0.001 s^{-1} to 0.01 s^{-1} but then shows an abrupt trend as it increases when strain rate is increased to 0.1 s^{-1}. The observed type of failure in those experiments show little ductility. Twinning appears to be the most active deformation mechanism (A. K. Rodriguez et al. 2013) at room temperature.

In Fig. 4.2 (b), the specimen temperature is increased to 100 °C, and the tensile test is carried while the temperature is maintained. Increased strain-rate sensitivity is visible across the strain rate decades. The plastic flow stress shows considerable change, and thermal softening is present beyond the ultimate tensile strength point. When comparing the 100 °C stress-strain curve to that of room temperature, the strain to fracture appears to be approximately doubled. Based on the instability in fracture at 0.1/s strain rate, the most likely deformation mechanism to occur is twinning. However, at slower deformations (0.001/s), the stress-strain behavior reflects the influence of grain nucleation and potential presence of other deformation mechanisms (Rodriguez et al., 2013, 2016).

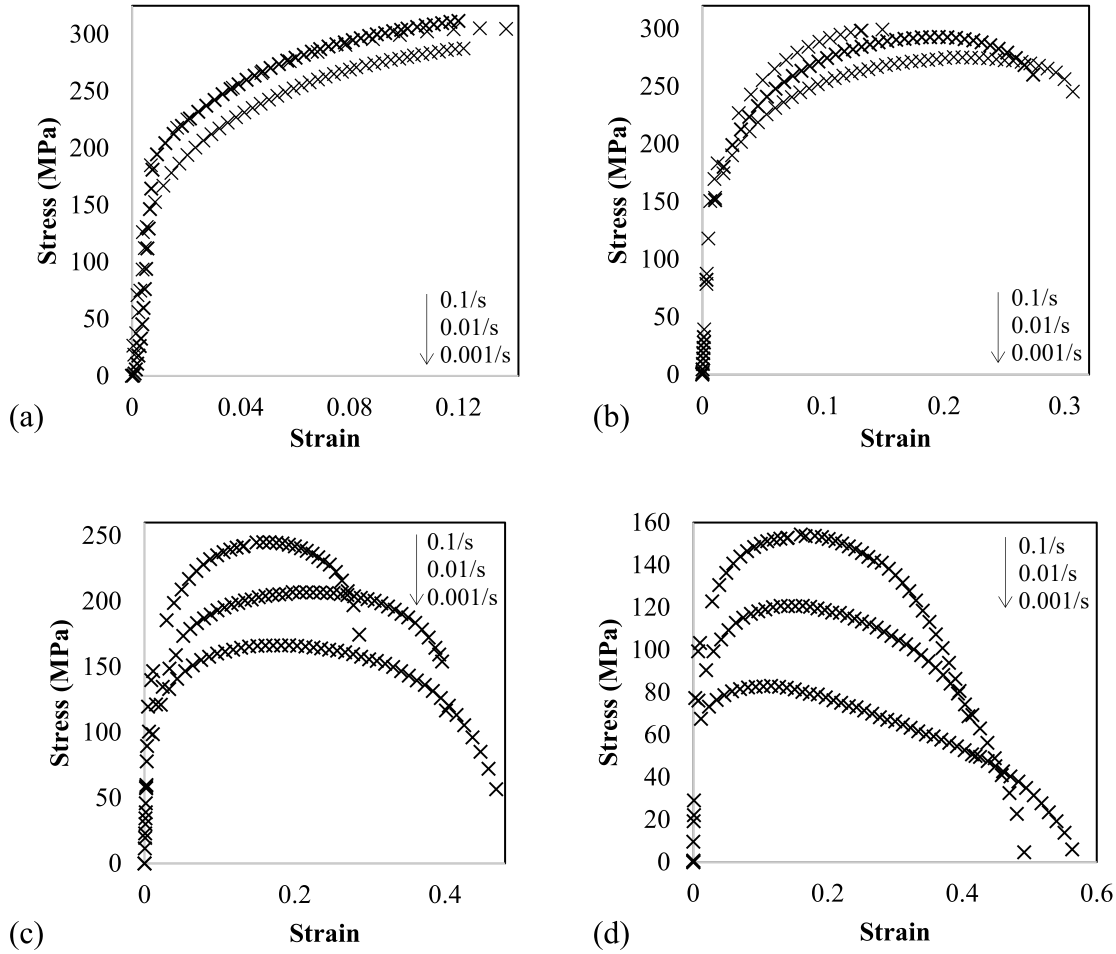

Fig. 4.1 – Uniaxial tensile Stress-strain curves at different strain rates for samples deformed at (a) 25 °C, (b) 100 °C, (c) 200 °C, (d) 300 °C

Upon carrying the tensile tests at elevated temperatures of 200 °C and 300 °C (Fig. 4.1 (c) and (d), respectively), a more pronounced strain rate effect is evident. In Fig. 4.1 (d), the results show the highest strain rate-dependency as to the material behavior with respect to strain rate. The 300 °C specimen shows up to 64% decrease in yield stress across the decreasing strain rate decades. However, the strain to fracture is significantly increased and reaches up to 58% at 0.001 /s. The strain rate effect is also pronounced on the decrease of the flow stress with decreasing strain rate. According to Rodriguez et al., this effect may be attributed to the occurrence of grain refinement and grain growth (including slipping, twinning and grain boundary sliding (GBS)); GBS likely appears to be the dominant deformation mechanism at 300 °C, especially at the smallest strain rate where there is less resistance to grain growth and longer time to achieve it (Rodriguez et al. 2016). In the microstructural analysis provided by the authors, an observation of smaller and more equiaxed grains is reported due to dynamic recrystallization (DRX) in the material, which is explanatory of the trends observed in the stress-strain curves of Fig. 4.1 (d), in particular.

4.2 Model Implementation and Parameter Identification

The monotonic stress-strain curves are used to calibrate the model parameters (Equations 3.16, 3.17 and 3.21). A transverse anisotropic stiffness tensor is used and the values of the five independent components are given by Simmons and Wang (Simmons and Wang, 1971) where $C_{11} = C_{22} = 58$ MPa; $C_{12} = 25$ MPa; $C_{13} = C_{23} = 20.8$ MPa; $C_{33} = 61.2$ MPa; $C_{44} = C_{55} = 16.6$ MPa. The TRC Mg AZ31B yielding anisotropy is represented using the Hill equivalent plastic stress (Eq. 11) and the values of the six Hill components are given by Jia and Bai (Jia and Bai, 2016) where F = 0.54, G = 0.74 and H = 0.26 (L = M = N = 1). The value of the parameter η appearing in the expression of the plastic characteristic tensor L^{d}_{ijkl} is assumed to be 0.25 (Chow et al., 1997).

The developed constitutive model features eight parameters controlling the plastic hardening, plasticity induced damage, strain rate sensitivity and ductility. The identification of the model parameters is conducted by finding the best agreement between the experimental and numerical stress-strain curves. At low temperatures, the strain rate sensitivity is little on the mechanical behavior of the alloy. Thus, the value for the strain sensitivity parameter m is chosen to be small. At 300 °C, the value for m is increased as the strain rate effect on the mechanical behavior is apparent. The specimen ductility, in the model, can be controlled by the initial resistance rates γ_p and γ_d, while the plastic hardening may be controlled by the power law parameters namely s_i^0, n^h and n^s. The mechanical behavior dependency on the test temperature is not explicitly accounted for in the model constitutive equations. Consequently, the modeling of the temperature effect on the mechanical behavior requires considering an evolution of some model parameters as a function of the temperature. Figure 4.2 shows the evolution of those parameters of which all the parameters are found to have a linear evolution except the strain hardening saturation parameter. The parameter identification is done separately for the stress strain curves at different temperatures. At room temperature, the specimens exhibit relatively low ductility that is slightly affected when strain rate is changed. This observation can be related to the limited number of slip systems that can be activated at room temperature and the activation of twinning (Koike et al., 2003). Thus, the material exhibits a semi-brittle behavior and shows little softening in the post-necking region. With increasing temperature, the ductility increases, particularly at 200 °C and 300 °C. (Rodriguez et al. 2013) and later (Ayoub et al. 2018) reported on the increasing activity of GBS with increasing temperature, as it can induce an acceleration of the dynamic recrystallization. The increase in the grain size (Rodriguez et al. 2013) especially at 300 °C explains the sudden drop of the hardening saturation limit s^s. The s^0 and s^s can be correlated with the critical resolved shear stress, which is a plasticity activation threshold that follows the Hall-Petch relationship. The continuous decrease of the initial shear strength resistance s^0 is associated with the decrease of the critical resolved shear stress needed to activate the different slip system with increasing temperatures (Ayoub et al. 2018).

As temperature increases, the initial plastic rate γ^p increases in value which in part increases the strain to fracture to accommodate the increase in ductility. The increase in the hardening parameter m is justified as the strain rate effect becomes pronounced significantly on the plastic flow and deformation with higher temperature. Observing the temperature effect on the plastic deformation, softening occurs at an expedited rate up to fracture. To accommodate this behavior, an increase in value of the hardening coefficient n^h is done which assists to achieve a rapid decrease in plastic hardening. As n^h was increased significantly at 300 °C, the effect can be directly reflected on the evolving hardening limit s^0 which reaches its saturation limit s^s at a steeper rate. In terms of damage, the parameter Y^0 is observed to decrease with increased temperature. This occurrence can be phenomenologically correlated with a decrease in damage strengthening. Recall that damage strengthening is a concept introduced by the authors (Hao et al., 1985) where they realize that the value of the damage strain energy release rate increases with the increase of the associated damage variables. This discussion closely applies to the trends observed for parameter n which is found to increase with temperature. As a rate dependent parameter, it is consistent with the increase of m, the plastic rate-sensitive parameter. The damage parameter γ^d is observed to have a direct effect on the strain to fracture; as it increases, the rate of damage increases which helps reduce the stress-strain curve elongation. Overall, it is important to note that the sets of identified model parameters for each temperature are not unique. However, they provide a starting point for a thorough identification processes. For this section, each of the parameters is plotted as a function of temperature. With regression, a fitting equation may be obtained to show the evolution of the parameters with respect to temperature. Knowing that the parameters evolve monotonically, an attempt is made to obtain a linear fit. The plots and regression equations are provided in Fig. 4.2.

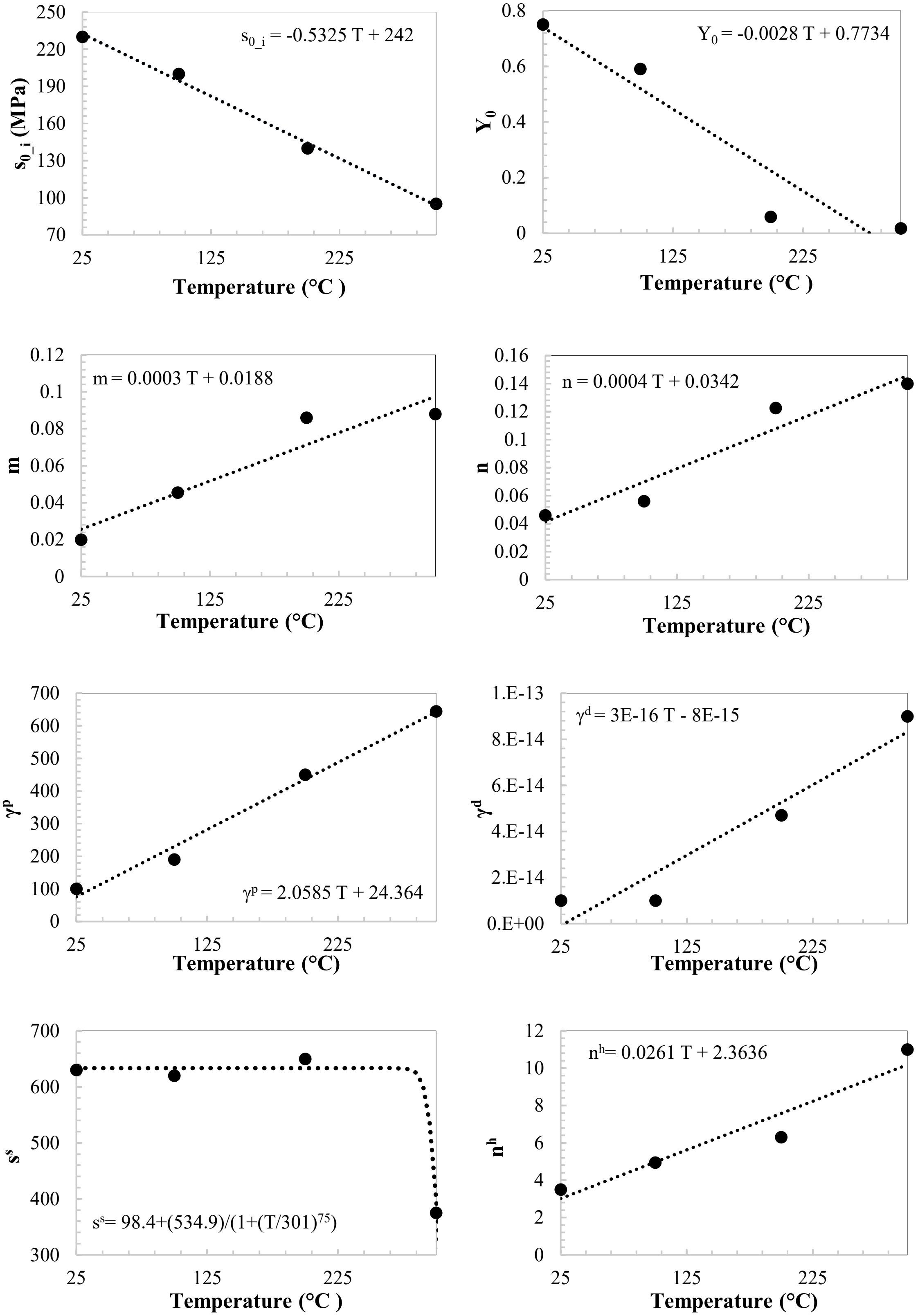

Fig. 4.2 – Evolution of the Plasticity and Damage Power Law Parameters

4.3 Numerical Prediction Analysis

In this section, the numerical predictions are compared with the experimental stress-strain curves. Using the identified parameters presented in the previous section, Figs. 4.3, 4.4, 4.5 and 4.6 present the predicted stress-strain curves that are plotted along with the experimental curves for different strain rates and temperatures. The corresponding numerical damage evolution are also plotted as a function of the strain.

The results show good agreement between the experimental stress-strain data and the numerical predictions. With increasing temperature, the model is able to predict the experimental behavior of the alloy in terms of yielding, hardening and softening up to the fracture limit. However, the numerical stress-strain curve at T=300°C and strain rate of 0.001/s, shows excessive hardening compared to experimental curve. Citing the earlier discussions for elevated temperatures, the material exhibits a major transition in its deformation mechanisms. The difference between the numerical predictions and the experimental observations in Figure 4.6 (a) is explained by a transition in the controlling deformation mechanisms: slip and some volume fraction of GBS to higher volume fraction of GBS, dynamic recrystallization and recovery (Rodriguez et al., 2013 and 2016). The combination of high temperature and lower strain rate (i.e. slow deformation) allows more time for the material to activate grain growth mechanisms. The pronounced strain softening may be attributed to the competition between grain refinement and grain growth that can be a clear indication of high angle grain boundary diffusion and/or grain-boundary sliding (GBS). It is believed that such micro-structural occurrences are the cause behind the significant drop in flow stress and in strain hardening. Overall, although the model lacks formulations for temperature influence, it is capable of predicting the mechanical properties of the alloy with an evolution of its parameters. The damage evolution curves shown in the below figures are related to the alloy stiffness degradation. The damage shows a nonlinear evolution. Initially, the damage evolves progressively with a slow rate (where the damage is very small) followed by a progressive increase in the rate indicating the initiation of softening which leads to fracture. It is worth noticing that the onset of plastic instability is coinciding with the increase in damage rate.

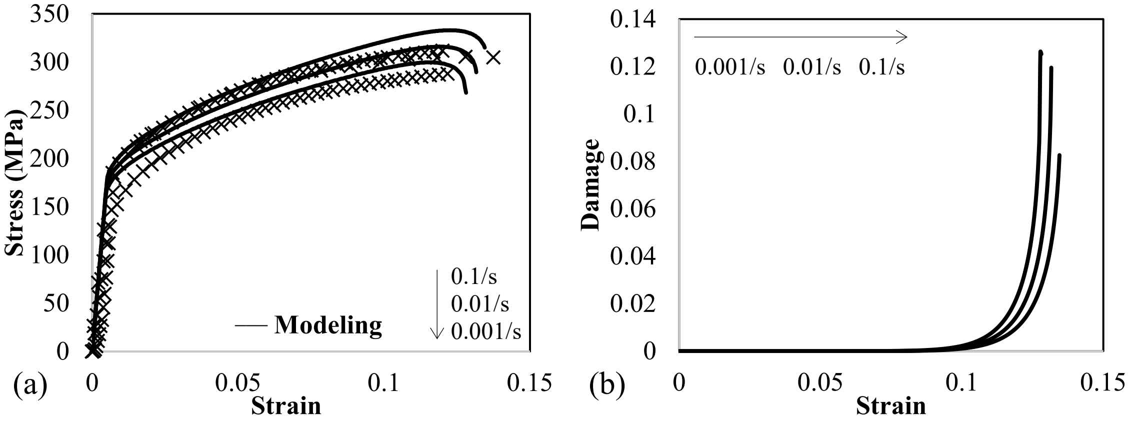

Fig. 4.3 – Model vs. Experimental Stress-strain Curves and Damage Evolution at T=25 °C

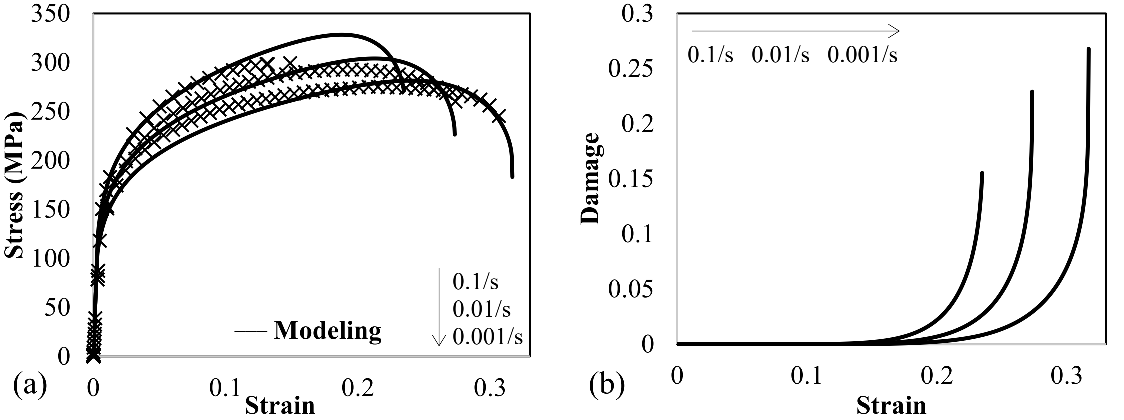

Fig. 4.4 – Model vs. Experimental Stress-strain Curves and Damage Evolution at T=100 °C

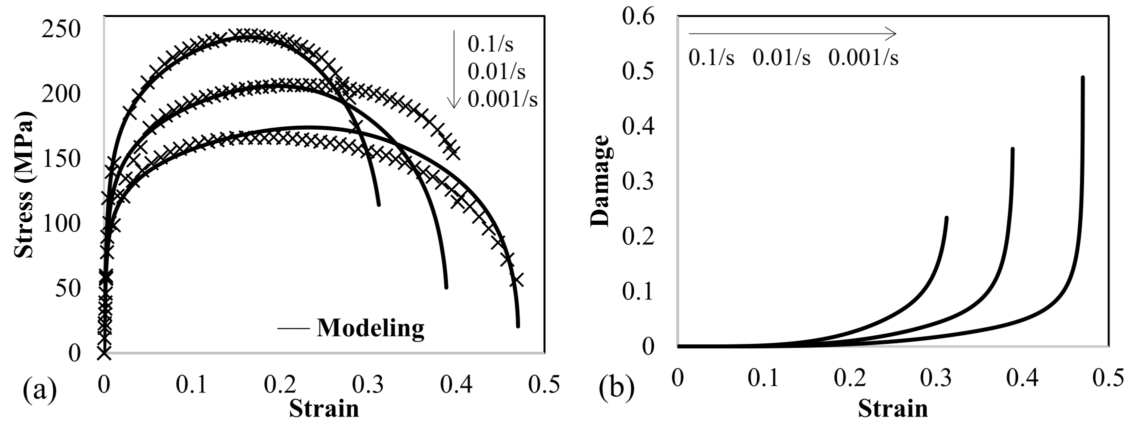

Fig. 4.5 – Model vs. Experimental Stress-strain Curves and Damage Evolution at T=200 °C

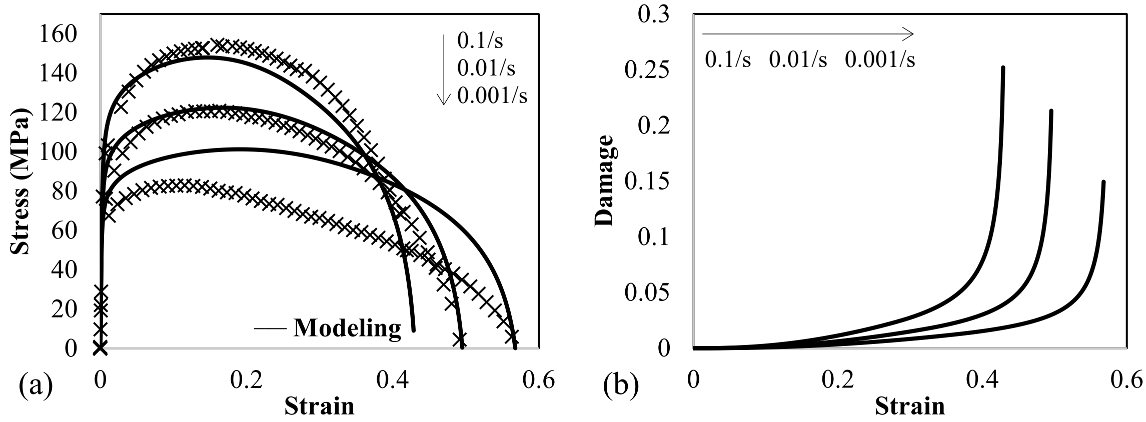

Fig. 4.6 – Model vs. Experimental Stress-strain Curves and Damage Evolution at T=300 °C

At this stress level, non-uniformity in plastic deformation occurs. This point is defined by the onset of diffuse necking, the same point where damage starts to pick up in value, which explains the non-linear evolution in the damage curves. The strain value at damage initiation corresponds to a critical damage value (Chow et al., 1997). At this point, the material exhibits plastic instability, and various damage mechanisms are activated. Schmitt and Jalinier describe two damaging processes that are active beyond this critical point: (1) damage by decohesion from the particle matrix interface that indicates the failure of a material particle and (2) damage by particle fragmentation which exhibits the nucleation and growth of damage with the formation of subsequent cracks (Schmitt and Jalinier, 1982). With the activation of damaging mechanisms, the damage value increases rapidly causing pronounced softening as shown in Fig. 4. This asymptotic increase in damage is reflected by the rapid loss of material stiffness associated with the growth, coalescence and formation of newer cracks. Initially, the values of the effective stress coincide with the values of the nominal stress up until necking. At the necking point, the effective stress diverts from the nominal stress and increases to infinity due to the decrease in the load bearing area. Note that the damage rupture values observed from the model are 20% on average across the temperatures. Overall, the damage values phenomenologically depict the combined effect of all concerned mechanisms on the material's softening behavior up until rupture.

The stress-strain curve of specimen tested at T=300°C and strain rate of 0.001 /s is now analyzed separately aiming to understand using simulations the underlying deformation mechanisms. A different set of model parameters is identified for a better prediction of the mechanical behavior. The parameters that provide the best fit of the experimental results are presented in Table 1. We can observe that the changes in the parameters values only concern the damage time dependent behavior described in Equation (3.21). The parameter n^h significantly increased in value to induce an increase in softening rate, so that the model captures the pronounced strain hardening reduction. The resulting numerical stress-strain and damage curves are presented in Fig. 5. The model shows a better prediction of the experimental data than the prediction presented previously in Fig 4.6 (a).

Table 1 – Suggested Model Parameters for T=300°C and $\dot{\varepsilon}$=0.001

Parameter	s^0	γ^p	m	n^s	n^h	Y^0	γ^d	n
Value	95	644	0.098	325	22	0.0173	1.5E-13	0.1211

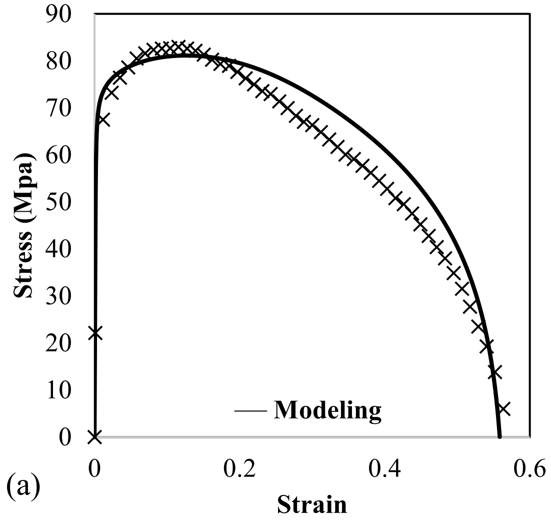

Fig. 4.7 – Updated Numerical vs. Experimental Stress-strain Curves and Damage Evolution Curve at 0.001 /s and T=300 °C

We aim to understand how n^h and the resultant evolution of parameter s affect the stress-strain response of the model. The set of parameters of Table 1 is considered. Fixing seven of the model parameters and reducing the value of the n^h from 22 to 11, we plot below the stress strain response compared with the experiment. We also plot the evolution of s as a function of the strain.

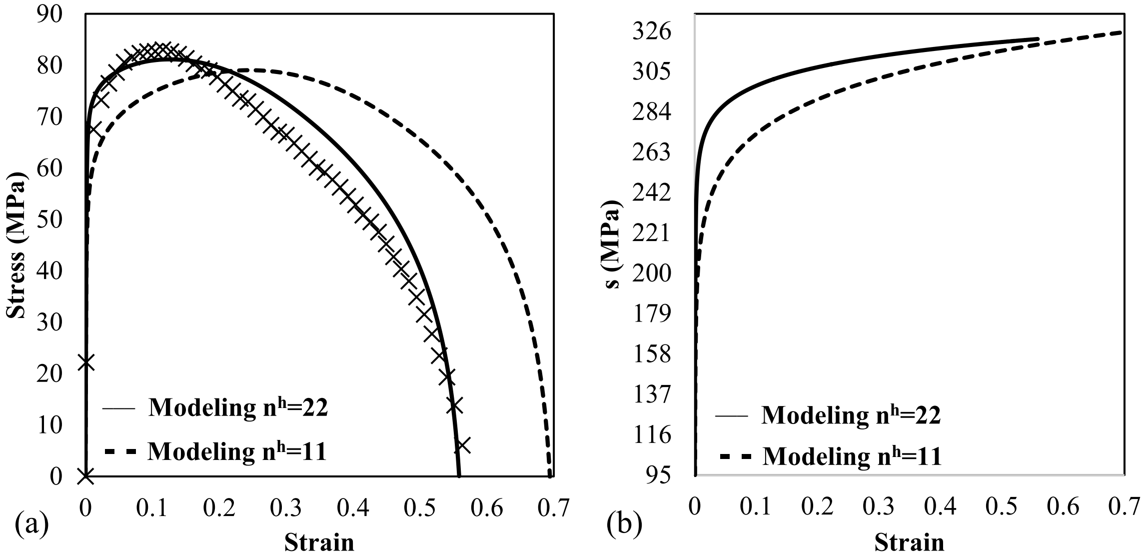

Fig. 4.8 – Demonstration of the Effect of n^h on Predicted Material Hardening

Observe how with a lower value for n^h, the shear resistance parameter s takes longer time to reach its saturation limit s^s. As a result, looking at the strain-rate response in Fig.6.a, the stress takes longer time to reach its ultimate value. Consequently, the predicted softening occurs at a later stage which explains the necessity to increase this parameter to accommodate the fast material softening behavior. Building on the discussions of section 4, the flow stress is significantly affected when the temperature is at T=300 °C and when a slow strain rate of 0.001/s is imposed. Looking at Fig.4.g, it is observed that the model does adjust for a reduction in flow stress. However, due to the complexity of the induced softening, the isotropic hardening saturation limit s^s of 375 MPa exaggerated the extent of hardening at the slow deformation. Thus, s^s is reduced to 325 MPa alongside an increase in the softening rate coefficient n^h from 11 to 22 so that the change is reflected on the predicted plastic flow stress and on the onset of softening. From this simulation, we deduce the increased sensitivity of the alloy to strain rate especially at elevated temperatures. This is in agreement with Dong et al. who report about the intensified dynamic softening effect on critical damage values of Mg AZ31B for the concerned temperature and loading rate; the authors find similar observations where elongation to fracture increases significantly at the reduced strain rate of 0.001/s and conclude this consequence to be due to the activation of non-basal slip systems (Dong et al., 2015). Wang et al. report on the increase in volume fraction of dynamic recrystallization grains as the strain rate is reduced to 0.001/s where the recrystallization behavior becomes intensified and original grains are surrounded and replaced by finer grains of recrystallization; the authors observed induced softening enhancement due to DRX and a reduction in stress concentration due to motion of dislocations (Wang et al., 2013). Ishikawa et al. studied the effect of strain rate on grain size for the alloy, whose observations indicated equiaxed and finer recrystallization grains (Ishikawa et al., 2005). This is in agreement with our discussion in section

4 as reported by (Ayoub et al., 2018b; Rodriguez et al., 2013) which also discuss the co-occurrence of GBS due to grain refinement. Thus, at elevated temperature and slower deformation rates, the activation of dynamic recrystallization increases the formability of the alloy. This is due to the improved plastic deformation capability assisted by the dominant presence of DRX mechanisms which significantly contribute to the improvement of material elongation at lower flow stresses. Correlating those phenomena to the model response, we recall that the theory of CDM does not resort to the micromechanical material analysis. Particularly in this model, the assumed damage evolution law evolves increasingly ignoring the effects of recrystallization. Thus, an incomplete reduction in flow stress was predicted by the model, for the unified use of the hardening parameters s^s and n^h. This justifies the need for a change to those parameters so that the effects of DRX may be manifested in the plastic evolution, in addition to the damage evolution, which can particularly be made to contribute to the intensified softening behavior in the predicted results.

In what follows, a quantitative assessment of the predicted mechanical properties is provided. For a thorough assessment of the model predictions, we compare the difference between the experimental and predicted mechanical properties such as work to fracture, yield stress, ultimate stress and strain to fracture. The comparisons are done in the plots against strain rate for all temperatures. The work of fracture is referred to as the fracture toughness of the material. The value of this energy may be obtained by integrating the area under the stress-strain curves up to the strain to failure (the values of work of fracture are expressed in MJ/m^3).

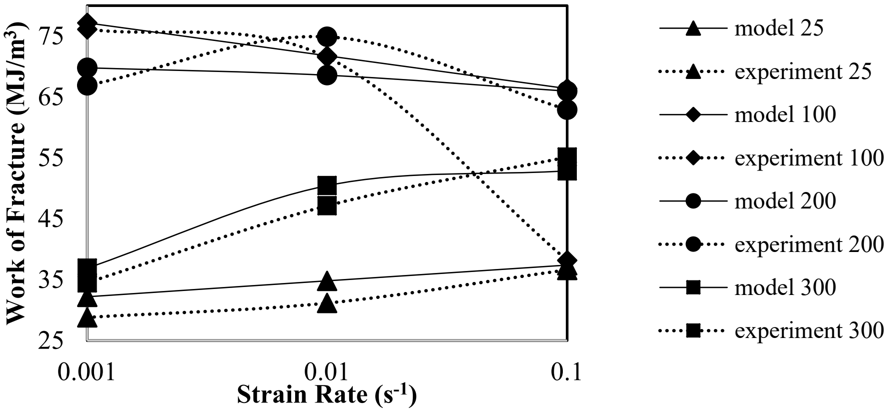

Fig. 4.9 – Work of Fracture vs. Strain Rate (Numerical Predictions vs. Experiments)

Fig. 4.9 presents the work of fracture versus strain rate at various temperatures; differences are observed in work of fracture for the temperature at 200 °C and strain rate of 0.01/s as well as temperature of 100 °C and strain rate of 0.1/s. In the former case, the constitutive model underestimates the work of fracture mainly due to the increased softening in the numerical stress-strain curve of Figure 4.e. This yields a lower area under the stress-strain curve explaining the reduced toughness. In the latter case, the experimental stress strain curve showed an abrupt and early fracture when compared to curves at 0.01/s and 0.001/s for the same temperature. Per the model observations, a more ductile and hardened material is predicted. Thus, the over-predicted toughness by the model is mainly influenced by the increase in ductility and increase in plastic hardening as compared to its experimental counterpart.

The evolution of the yield stress versus strain rate at different temperatures is presented in Fig. 4.10. The yield stress values are within acceptable variability between the experiments and numerical predictions. Note that all yield stress values are determined by the 0.2% offset method.

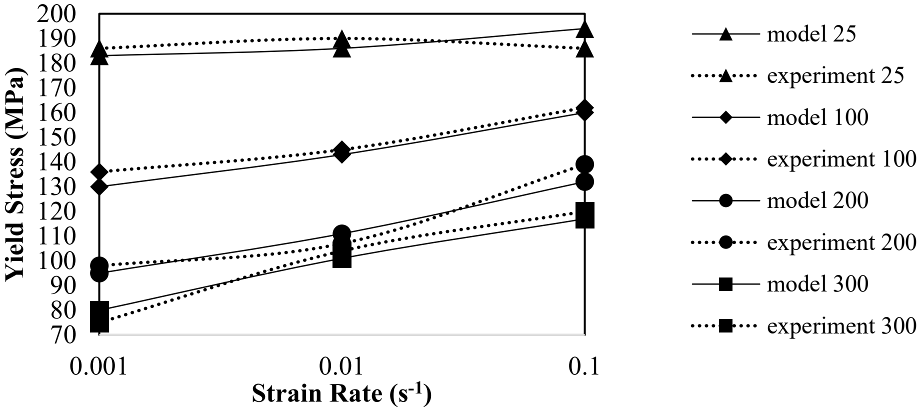

Fig. 4.10 – Yield Stress vs. Strain Rate (Numerical Predictions vs. Experiments)

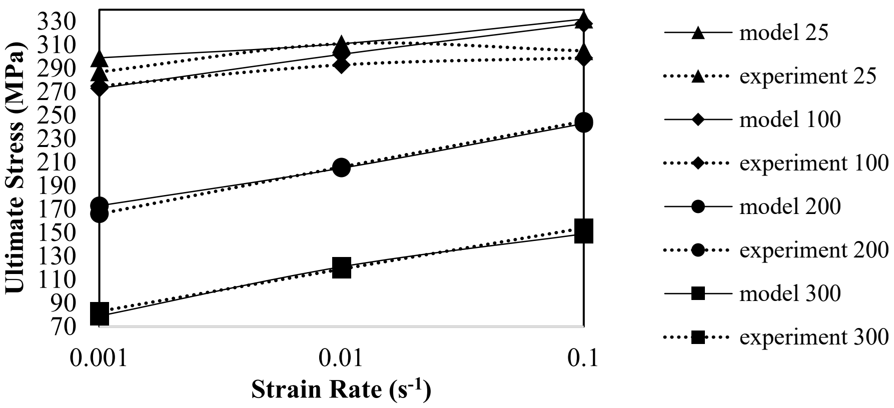

Fig. 4.11 – Ultimate Stress vs. Strain Rate (Numerical Predictions vs. Experiments)

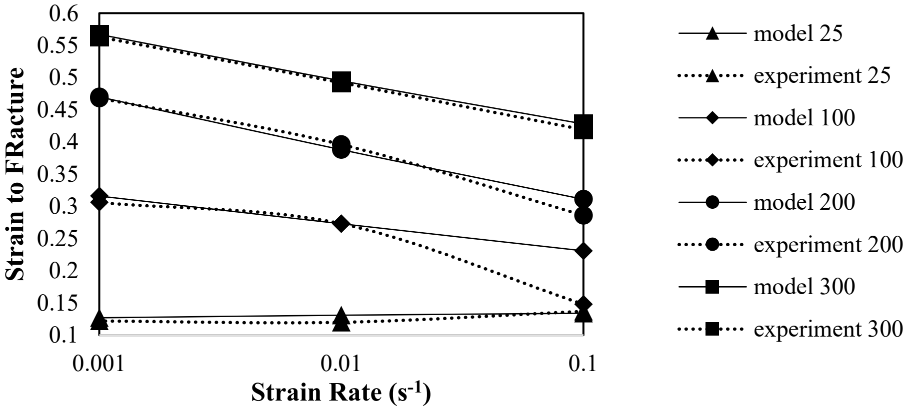

Fig. 4.12 – Strain to Fracture vs. Strain Rate (Numerical Predictions vs. Experiments)

Fig. 4.11 presents the ultimate stress in function of strain rate at different temperatures. At temperature of 25 °C and strain rate of 0.1/s, the model showed a higher ultimate stress of 332 MPa compared to 302 MPa exhibited by the experiments. This is mainly due to the diminished strain rate sensitivity effect on the mechanical behavior of the alloy at low temperatures. Moreover, the alloy shows reduced deformation stability at low temperature due to dislocation climb and inactivation of major deformation mechanisms. With that, the exaggerated model value may be justified. At temperature of 100 °C and strain rate of 0.1/s, the predicted ultimate stress is 328 MPa which is higher than 299 MPa according to the experiment. This is relevant to the decreased plastic deformation capability at higher strain rate of 0.1/s. The experimental stress-strain curve did not show any major hardening on the behavior. As such, a lower experimental ultimate stress value is expected.

Fig. 4.12 presents the evolution of the strain to fracture as a function of strain rate at different temperatures. At temperature of 100 °C and strain rate of 0.1/s, the predicted strain to fracture is 0.231 which is higher than its experimental value of 0.148. This is due to the early fracture of the material in the conducted experiments which is relevant to the diminished plastic deformation and instability.

Overall, the reported material characteristics are in considerable agreement between the model and experiments. This concludes the model performance evaluation.

4.4 References

Antoniswamy, A.R., Weldon, A.J., Taleff, E.M., Hector, L.G., Carter, J.T., 2016. Hot Forming of Mg AZ31B Alloy Sheet Processed by Warm Rolling. Mater. Sci. Forum 838–839, 157–165. https://doi.org/10.4028/www.scientific.net/MSF.838-839.157

Ayoub, G., A. K. Rodrigez, M. Shehadeh, G. Kridli, J. P. Young, and H. Zbib. 2018. "Modelling the Rate and Temperature-Dependent Behaviour and Texture Evolution of the Mg AZ31B Alloy TRC Sheets." *Philosophical Magazine* 98 (4): 262–94. https://doi.org/10.1080/14786435.2017.1403054.

Bussiba, A., Ben Artzy, A., Shtechman, A., Ifergan, S., Kupiec, M., 2001. Grain refinement of AZ31 and ZK60 Mg alloys - Towards superplasticity studies. Mater. Sci. Eng. A 302, 56–62. https://doi.org/10.1016/S0921-5093(00)01354-X

Chino, Yasumasa, Katsuya Kimura, and Mamoru Mabuchi. 2008. "Twinning Behavior and Deformation Mechanisms of Extruded AZ31 Mg Alloy." *Materials Science and Engineering A* 486 (1–2): 481–88. https://doi.org/10.1016/j.msea.2007.09.058.

Chow, C. L., L. G. Yu, and M. Y. Demeri. 1997. "A Unified Damage Approach for Predicting Forming Limit Diagrams." *Journal of Engineering Materials and Technology* 119 (4). American Society of Mechanical Engineers: 346. https://doi.org/10.1115/1.2812269.

Dong, J.R., Zhang, D.F., Dong, Y.F., Pan, F.S., Chai, S.-S., 2015. Critical damage value of AZ31B magnesium alloy with different temperatures and strain rates. Rare Met. 1–6. https://doi.org/10.1007/s12598-014-0440-y

Hao, Lee, Peng Ke, and Wang June. 1985. "An Anisotropic Damage Criterion for Deformation Instability and Its Application to Forming Limit Analysis of Metal Plates." *Engineering Fracture Mechanics* 21 (5): 1031–54. https://doi.org/10.1016/0013-7944(85)90008-6.

Ishikawa, K., Watanabe, H., Mukai, T., 2005. High temperature compressive properties over a wide range of strain rates in an AZ31 magnesium alloy. J. Mater. Sci. 40, 1577–1582. https://doi.org/10.1007/s10853-005-0656-1

Jia, Yueqian, and Yuanli Bai. 2016. "Experimental Study on the Mechanical Properties of AZ31B-H24 Magnesium Alloy Sheets under Various Loading Conditions." *International Journal of Fracture* 197 (1): 25–48. https://doi.org/10.1007/s10704-015-0057-7.

Koike, J., R. Ohyama, T. Kobayashi, M. Suzuki, and K. Maruyama. 2003. "Grain-Boundary Sliding in AZ31 Magnesium Alloys at Room Temperature to 523 K." *MATERIALS TRANSACTIONS* 44 (4): 445–51. https://doi.org/10.2320/matertrans.44.445.

Kronenburg, M. J. 2013. "A Method for Fast Diagonalization of a 2x2 or 3x3 Real Symmetric Matrix," June. http://arxiv.org/abs/1306.6291.

Lemaitre, Jean. 1996. *A Course on Damage Mechanics*. Berlin, Heidelberg: Springer Berlin Heidelberg. https://doi.org/10.1007/978-3-642-18255-6.

Rodriguez, A. K., G. Kridli, G Ayoub, and H. Zbib. 2013. "Effects of the Strain Rate and Temperature on the Microstructural Evolution of Twin-Rolled Cast Wrought AZ31B Alloys

Sheets." *Journal of Materials Engineering and Performance* 22 (10). Springer US: 3115–25. https://doi.org/10.1007/s11665-013-0598-8.

Rodriguez, A.K., G.A. Ayoub, B. Mansoor, and A.A. Benzerga. 2016. "Effect of Strain Rate and Temperature on Fracture of Magnesium Alloy AZ31B." *Acta Materialia* 112: 194–208. https://doi.org/10.1016/j.actamat.2016.03.061.

Schmitt, J.H., Jalinier, J.M., 1982. Damage in sheet metal forming—I. Physical behavior. Acta Metall. 30, 1789–1798. https://doi.org/10.1016/0001-6160(82)90095-5

Wang, L., Huang, G., Li, H., Zhang, H., 2013. Influence of strain rate on microstructure and formability of AZ31B magnesium alloy sheets. Trans. Nonferrous Met. Soc. China 23, 916–922. https://doi.org/10.1016/S1003-6326(13)62548-0

CHAPTER 5
CONCLUSIONS AND FUTURE WORK

5.1 Summary of Contributions

In this work, an anisotropic and time-dependent damage-coupled plasticity model is developed to predict the viscoplastic behavior of ductile alloys under large deformations. The development is done in arbitrary coordinate space to accommodate both proportional and non-proportional service loadings. This research piece presents a novel and practical implementation in continuum mechanics to model the post-necking (softening) behavior that is induced by damage accounting to the reduction in material stiffness. Unlike previous CDM implementations, this work addresses the implementation of rate-dependent plasticity and damage evolution formulations to respond to changes in material's behavior when loading strain rate is varied.

For the anisotropic implementation under finite deformation, an implicit numerical scheme was developed to solve for the model rate equations. The choice of an implicit scheme is to eliminate stability limits and suit compatibility for UMAT subroutine writings. With the proven applicability of this arbitrary framework development, this thesis contributions may be summarized by the model's

1. Excellent performance in capturing the anisotropic and time-dependent stress-strain response of Mg AZ31B and potentially other ductile alloys such as steel and aluminum

2. Capability of modeling the post-necking damage influence on the stress strain response until fracture by accounting to the reduction in material load bearing capability, thus the degraded elastic modulus
3. Offering a computationally efficient numerical method which reduces simulation time in further research works, especially when coupled for finite element simulations of bigger structures
4. Mathematical model scheme capability to capture the strain rate effect on the material's mechanical response and precisely approximate the yield stress, ultimate tensile strength and the strain to fracture
5. Employability in automotive stamping applications to help fulfil the light-weighting desire of automotive panels, which requires analyzing the complex behaviors of non-conventional alloys

5.2 Future Directions

Future work addresses the implementation of the constitutive equations in UMAT for utilization in finite element. The ultimate goal behind this model is to provide a computationally efficient numerical tool which allows the modeling of damage in alloys and obtaining a realistic stress-strain response while accounting to the degradation in material mechanical properties. Since the model is developed for an arbitrary coordinate space, validation for the three-dimensional case is sought in future work where with finite element implementation, a realistic 3D loading can be imposed on the deformation gradient. In addition, relevant to the strain-sensitive features of this model development, the investigation and validation for other viscoplastic materials may be considered.

APPENDIX I
ON THE DIAGONALIZATION OF Y_{ij}

A. Eigenvalues of Y

The Characteristic Equation for Y is: $\lambda^3 - b\lambda^2 + c\lambda + d = 0$

where

$$b = Y_{11} + Y_{22} + Y_{33}$$

$$c = Y_{11}Y_{22} + Y_{11}Y_{33} + Y_{22}Y_{33} - Y_{12}^2 - Y_{13}^2 - Y_{23}^2$$

$$d = Y_{11}Y_{23}^2 + Y_{22}Y_{13}^2 + Y_{33}Y_{12}^2 - Y_{11}Y_{22}Y_{33} - 2Y_{12}Y_{13}Y_{23}$$

Denote

$$p = b^2 - 3c$$

$$q = 2b^3 - 9bc - 27d$$

The discriminant for the 3rd order polynomial is written as: $\Delta = \cos^{-1}\left(\dfrac{q}{2\sqrt{p^3}}\right)$

Note that when $q^2 < 4p^3$ there exist 3 real distinct roots

$$\lambda_1 = \frac{1}{3}\left[b + 2\sqrt{p}\cos\left(\tfrac{1}{3}\Delta\right)\right]$$

$$\lambda_2 = \frac{1}{3}\left[b + 2\sqrt{p}\cos\left(\tfrac{1}{3}\Delta + \tfrac{2\pi}{3}\right)\right]$$

$$\lambda_3 = \frac{1}{3}\left[b + 2\sqrt{p}\cos\left(\tfrac{1}{3}\Delta - \tfrac{2\pi}{3}\right)\right]$$

B. Inner Derivatives

Let $u = \frac{q}{2\sqrt{p^3}}$, then $\Delta = \cos^{-1} u$

Since Δ is a composition of two function, using the chain rule we calculate

$$\frac{\partial \Delta}{\partial D} = \frac{\partial \Delta}{\partial u}\frac{\partial u}{\partial D}$$

where $\frac{\partial \Delta}{\partial u} = -\frac{1}{\sqrt{1-u^2}}$

and $$\frac{\partial u}{\partial D} = \frac{\frac{\partial q}{\partial D}\left[2\sqrt{p^3}\right] - 2q\left[1.5p^{1/2}\frac{\partial p}{\partial D}\right]}{4p^3} = \frac{\frac{\partial q}{\partial D}\left[\sqrt{p^3}\right] - 1.5p^{1/2}q\left[\frac{\partial p}{\partial D}\right]}{2p^3}$$

such that

$$\frac{\partial p}{\partial D} = 2b\frac{\partial b}{\partial D} - 3\frac{\partial c}{\partial D}$$

$$\frac{\partial q}{\partial D} = 6b^2\frac{\partial b}{\partial D} - 9\left(c\frac{\partial b}{\partial D} + b\frac{\partial c}{\partial D}\right) - 27\frac{\partial d}{\partial D}$$

where

$$\frac{\partial b}{\partial D} = \frac{\partial Y_{11}}{\partial D} + \frac{\partial Y_{22}}{\partial D} + \frac{\partial Y_{33}}{\partial D}$$

$$\frac{\partial c}{\partial D} = Y_{22}\frac{\partial Y_{11}}{\partial D} + Y_{11}\frac{\partial Y_{22}}{\partial D} + Y_{33}\frac{\partial Y_{11}}{\partial D} + Y_{11}\frac{\partial Y_{33}}{\partial D} + Y_{33}\frac{\partial Y_{22}}{\partial D} + Y_{22}\frac{\partial Y_{33}}{\partial D} - 2Y_{12}\frac{\partial Y_{12}}{\partial D} - 2Y_{13}\frac{\partial Y_{13}}{\partial D} - 2Y_{23}\frac{\partial Y_{23}}{\partial D}$$

$$\begin{aligned}\frac{\partial d}{\partial D} &= 2Y_{11}Y_{23}\frac{\partial Y_{23}}{\partial D} + Y_{23}^2\frac{\partial Y_{11}}{\partial D} + 2Y_{22}Y_{13}\frac{\partial Y_{13}}{\partial D} + Y_{13}^2\frac{\partial Y_{22}}{\partial D} + 2Y_{33}Y_{12}\frac{\partial Y_{12}}{\partial D} + Y_{12}^2\frac{\partial Y_{33}}{\partial D}\\ &-\left(\frac{\partial Y_{11}}{\partial D}Y_{22}Y_{33} + Y_{11}\frac{\partial Y_{22}}{\partial D}Y_{33} + Y_{11}Y_{22}\frac{\partial Y_{33}}{\partial D}\right)\\ &-2\left(\frac{\partial Y_{12}}{\partial D}Y_{13}Y_{23} + Y_{12}\frac{\partial Y_{13}}{\partial D}Y_{23} + Y_{12}Y_{13}\frac{\partial Y_{23}}{\partial D}\right)\end{aligned}$$

C. Trigonometric Identities

$\cos(-\alpha) = \cos\alpha$; $\sin(-\alpha) = -\sin\alpha$

Derive the cosine functions as written below

$$\frac{\partial \cos\left(\frac{1}{3}\Delta\right)}{\partial D} = -\sin\left(\tfrac{1}{3}\Delta\right) * \frac{1}{3} * \frac{\partial \Delta}{\partial D}; \quad \frac{\partial \sin\left(\frac{1}{3}\Delta\right)}{\partial D} = \cos\left(\tfrac{1}{3}\Delta\right) * \frac{1}{3} * \frac{\partial \Delta}{\partial D}$$

$$\frac{\partial \cos\left(\frac{1}{3}\Delta + \frac{2\pi}{3}\right)}{\partial D} = -\sin\left(\tfrac{1}{3}\Delta + \tfrac{2\pi}{3}\right) * \frac{1}{3} * \frac{\partial \Delta}{\partial D}; \quad \frac{\partial \cos\left(\frac{1}{3}\Delta - \frac{2\pi}{3}\right)}{\partial D} = -\sin\left(\tfrac{1}{3}\Delta - \tfrac{2\pi}{3}\right) * \frac{1}{3} * \frac{\partial \Delta}{\partial D}$$

D. Derivatives of the Eigenvalues of Y

The derivatives of the eigenvalues of Y with respect to the damage are calculated below. We may calculate the derivatives with respect to the stress similarly.

$$\frac{\partial \lambda_1}{\partial D} = \frac{1}{3}\left[\frac{\partial b}{\partial D} + \frac{1}{\sqrt{p}}\frac{\partial p}{\partial D}\cos\left(\tfrac{1}{3}\Delta\right) + 2\sqrt{p}\,\frac{\partial \cos\left(\frac{1}{3}\Delta\right)}{\partial D}\right]$$

$$\frac{\partial \lambda_2}{\partial D} = \frac{1}{3}\left[\frac{\partial b}{\partial D} + \frac{1}{\sqrt{p}}\frac{\partial p}{\partial D}\cos\left(\tfrac{1}{3}\Delta + \tfrac{2\pi}{3}\right) + 2\sqrt{p}\,\frac{\partial \cos\left(\frac{1}{3}\Delta + \frac{2\pi}{3}\right)}{\partial D}\right]$$

$$\frac{\partial \lambda_3}{\partial D} = \frac{1}{3}\left[\frac{\partial b}{\partial D} + \frac{1}{\sqrt{p}}\frac{\partial p}{\partial D}\cos\left(\tfrac{1}{3}\Delta - \tfrac{2\pi}{3}\right) + 2\sqrt{p}\,\frac{\partial \cos\left(\frac{1}{3}\Delta - \frac{2\pi}{3}\right)}{\partial D}\right]$$

APPENDIX II
DETERMINATION OF THE STRESS AND DAMAGE RATE TENSORS

A. Determining the Stress Rates

Having identified the damage effect tensor in Chapter 3, the effective Hill tensor is obtained

$$\tilde{\boldsymbol{H}} = \boldsymbol{M}^{T}(\boldsymbol{D}) : \boldsymbol{H} : \boldsymbol{M}(\boldsymbol{D})$$

which may be expressed in matricial form such that

$$\tilde{\boldsymbol{H}} = \begin{pmatrix} \frac{G+H}{(1-D_{11})^2} & \frac{-H}{(1-D_{11})(1-D_{22})} & \frac{-G}{(1-D_{11})(1-D_{33})} & 0 & 0 & 0 \\ \frac{-H}{(1-D_{11})(1-D_{22})} & \frac{H+F}{(1-D_{22})^2} & \frac{-F}{(1-D_{22})(1-D_{33})} & 0 & 0 & 0 \\ \frac{-G}{(1-D_{11})(1-D_{33})} & \frac{-F}{(1-D_{22})(1-D_{33})} & \frac{F+G}{(1-D_{33})^2} & 0 & 0 & 0 \\ 0 & 0 & 0 & \frac{2L}{(1-D_{22})(1-D_{33})} & 0 & 0 \\ 0 & 0 & 0 & 0 & \frac{2M}{(1-D_{33})(1-D_{11})} & 0 \\ 0 & 0 & 0 & 0 & 0 & \frac{2N}{(1-D_{11})(1-D_{22})} \end{pmatrix}$$

Intermediately, we find the double index contraction of the effective Hill tensor and the Stress tensor as expressed below

$$\tilde{\boldsymbol{H}} : \boldsymbol{S} = \begin{pmatrix} \frac{G+H}{(1-D_{11})^2} & \frac{-H}{(1-D_{11})(1-D_{22})} & \frac{-G}{(1-D_{11})(1-D_{33})} & 0 & 0 & 0 \\ \frac{-H}{(1-D_{11})(1-D_{2})} & \frac{H+F}{(1-D_{22})^2} & \frac{-F}{(1-D_{22})(1-D_{33})} & 0 & 0 & 0 \\ \frac{-G}{(1-D_{11})(1-D_{33})} & \frac{-F}{(1-D_{22})(1-D_{33})} & \frac{F+G}{(1-D_{33})^2} & 0 & 0 & 0 \\ 0 & 0 & 0 & \frac{2L}{(1-D_{22})(1-D_{33})} & 0 & 0 \\ 0 & 0 & 0 & 0 & \frac{2M}{(1-D_{33})(1-D_{11})} & 0 \\ 0 & 0 & 0 & 0 & 0 & \frac{2N}{(1-D_{11})(1-D_{22})} \end{pmatrix} \begin{pmatrix} S_{11} \\ S_{22} \\ S_{33} \\ S_{23} \\ S_{13} \\ S_{12} \end{pmatrix}$$

$$
= \begin{pmatrix}
S_{11}\frac{G+H}{(1-D_{11})^2} + S_{22}\frac{-H}{(1-D_{11})(1-D_{22})} + S_{33}\frac{-G}{(1-D_{11})(1-D_{33})} \\
S_{11}\frac{-H}{(1-D_{11})(1-D_{22})} + S_{22}\frac{H+F}{(1-D_{22})^2} + S_{33}\frac{-F}{(1-D_{22})(1-D_{33})} \\
S_{11}\frac{-G}{(1-D_{11})(1-D_{33})} + S_{22}\frac{-F}{(1-D_{22})(1-D_{33})} + S_{33}\frac{F+G}{(1-D_{33})^2} \\
S_{23}\frac{2L}{(1-D_{22})(1-D_{33})} \\
S_{13}\frac{2M}{(1-D_{33})(1-D_{11})} \\
S_{12}\frac{2N}{(1-D_{11})(1-D_{22})}
\end{pmatrix}
$$

The equivalent stress is defined as

$$
\tilde{S}_{eq} = (\tfrac{1}{2}\boldsymbol{S}:\tilde{\boldsymbol{H}}:\boldsymbol{S})^{1/2} = \begin{pmatrix}
\frac{S_{11}}{2}\left(S_{11}\frac{G+H}{(1-D_{11})^2} + S_{22}\frac{-H}{(1-D_{11})(1-D_{22})} + S_{33}\frac{-G}{(1-D_{11})(1-D_{33})}\right) \\
+\frac{S_{22}}{2}\left(S_{11}\frac{-H}{(1-D_{11})(1-D_{22})} + S_{22}\frac{H+F}{(1-D_{22})^2} + S_{33}\frac{-F}{(1-D_{22})(1-D_{33})}\right) \\
+\frac{S_{33}}{2}\left(S_{11}\frac{-G}{(1-D_{11})(1-D_{33})} + S_{22}\frac{-F}{(1-D_{22})(1-D_{33})} + S_{33}\frac{F+G}{(1-D_{33})^2}\right) \\
+S_{23}^2\frac{L}{(1-D_{22})(1-D_{33})} + S_{13}^2\frac{M}{(1-D_{33})(1-D_{11})} + S_{12}^2\frac{N}{(1-D_{11})(1-D_{22})}
\end{pmatrix}^{1/2}
$$

The plastic power law may be calculated, and we derive obtain the plastic rate of deformation

$$
\dot{\boldsymbol{E}}^{\boldsymbol{p}} = \frac{\dot{p}}{2\tilde{S}_{eq}}\tilde{\boldsymbol{H}}:\boldsymbol{S} = \frac{\gamma_0(\frac{1}{s})^{1/m}\left(\tilde{S}_{eq}\right)^{1/m}}{2\tilde{S}_{eq}}\tilde{\boldsymbol{H}}:\boldsymbol{S}
$$

$$
= \frac{\gamma_0}{2}(\tfrac{1}{s})^{1/m}\left(\tilde{S}_{eq}\right)^{\frac{1-m}{m}}\tilde{\boldsymbol{H}}:\boldsymbol{S}
$$

Denote

$$
\omega = \frac{\dot{p}}{2\tilde{S}_{eq}} = \frac{1}{2}\gamma_0(\tfrac{1}{s})^{1/m}\left(\tilde{S}_{eq}\right)^{\frac{1-m}{m}}
$$

Now find the elastic rate of deformation

$$
\dot{E}_{11}^e = \dot{E}_{11} - \omega\left(S_{11}\frac{G+H}{(1-D_{11})^2} + S_{22}\frac{-H}{(1-D_{11})(1-D_{22})} + S_{33}\frac{-G}{(1-D_{11})(1-D_{33})}\right)
$$

$$
\dot{E}_{22}^e = \dot{E}_{22} - \omega\left(S_{11}\frac{-H}{(1-D_{11})(1-D_{22})} + S_{22}\frac{H+F}{(1-D_{22})^2} + S_{33}\frac{-F}{(1-D_{22})(1-D_{33})}\right)
$$

$$\dot{E}^{e}_{33} = \dot{E}_{33} - \omega\left(S_{11}\,\tfrac{-G}{(1-D_{11})(1-D_{33})} + S_{22}\,\tfrac{-F}{(1-D_{22})(1-D_{33})} + S_{33}\,\tfrac{F+G}{(1-D_{33})^{2}} \right)$$

$$\dot{E}^{e}_{23} = \dot{E}_{23} - \omega\left(S_{23}\,\tfrac{2L}{(1-D_{22})(1-D_{33})} \right)$$

$$\dot{E}^{e}_{13} = \dot{E}_{13} - \omega\left(S_{13}\,\tfrac{2M}{(1-D_{33})(1-D_{11})} \right)$$

$$\dot{E}^{e}_{12} = \dot{E}_{12} - \omega\left(S_{12}\,\tfrac{2N}{(1-D_{11})(1-D_{22})} \right)$$

Then, obtain the stress rates as expressed below

$$\dot{\boldsymbol{S}} = \tilde{\boldsymbol{C}} : \left(\dot{\boldsymbol{E}} - \dot{\boldsymbol{E}}^{p} \right)$$

$$\dot{S}_{11} = \left\{ \begin{array}{l} C_{1111}(1-D_{11})^{2} * \left[\dot{E}_{11} - \omega\left(S_{11}\,\tfrac{G+H}{(1-D_{11})^{2}} + S_{22}\,\tfrac{-H}{(1-D_{11})(1-D_{22})} + S_{33}\,\tfrac{-G}{(1-D_{11})(1-D_{33})} \right) \right] \\ +C_{1122}(1-D_{11})(1-D_{22}) * \left[\dot{E}_{22} - \omega\left(S_{11}\,\tfrac{-H}{(1-D_{11})(1-D_{22})} + S_{22}\,\tfrac{H+F}{(1-D_{22})^{2}} + S_{33}\,\tfrac{-F}{(1-D_{22})(1-D_{33})} \right) \right] \\ +C_{1133}(1-D_{11})(1-D_{33}) * \left[\dot{E}_{33} - \omega\left(S_{11}\,\tfrac{-G}{(1-D_{11})(1-D_{33})} + S_{22}\,\tfrac{-F}{(1-D_{22})(1-D_{33})} + S_{33}\,\tfrac{F+G}{(1-D_{33})^{2}} \right) \right] \end{array} \right\}$$

$$\dot{S}_{22} = \left\{ \begin{array}{l} C_{2211}(1-D_{11})(1-D_{22}) * \left[\dot{E}_{11} - \omega\left(S_{11}\,\tfrac{G+H}{(1-D_{11})^{2}} + S_{22}\,\tfrac{-H}{(1-D_{11})(1-D_{22})} + S_{33}\,\tfrac{-G}{(1-D_{11})(1-D_{33})} \right) \right] \\ +C_{2222}(1-D_{22})^{2} * \left[\dot{E}_{22} - \omega\left(S_{11}\,\tfrac{-H}{(1-D_{11})(1-D_{22})} + S_{22}\,\tfrac{H+F}{(1-D_{22})^{2}} + S_{33}\,\tfrac{-F}{(1-D_{22})(1-D_{33})} \right) \right] \\ +C_{2233}(1-D_{22})(1-D_{33}) * \left[\dot{E}_{33} - \omega\left(S_{11}\,\tfrac{-G}{(1-D_{11})(1-D_{33})} + S_{22}\,\tfrac{-F}{(1-D_{22})(1-D_{33})} + S_{33}\,\tfrac{F+G}{(1-D_{33})^{2}} \right) \right] \end{array} \right\}$$

$$\dot{S}_{33} = \left\{ \begin{array}{l} C_{3311}(1-D_{11})(1-D_{33}) * \left[\dot{E}_{11} - \omega\left(S_{11}\,\tfrac{G+H}{(1-D_{11})^{2}} + S_{22}\,\tfrac{-H}{(1-D_{11})(1-D_{22})} + S_{33}\,\tfrac{-G}{(1-D_{11})(1-D_{33})} \right) \right] \\ +C_{3322}(1-D_{22})(1-D_{33}) * \left[\dot{E}_{22} - \omega\left(S_{11}\,\tfrac{-H}{(1-D_{11})(1-D_{22})} + S_{22}\,\tfrac{H+F}{(1-D_{22})^{2}} + S_{33}\,\tfrac{-F}{(1-D_{22})(1-D_{33})} \right) \right] \\ +C_{3333}(1-D_{33})^{2} * \left[\dot{E}_{33} - \omega\left(S_{11}\,\tfrac{-G}{(1-D_{11})(1-D_{33})} + S_{22}\,\tfrac{-F}{(1-D_{22})(1-D_{33})} + S_{33}\,\tfrac{F+G}{(1-D_{33})^{2}} \right) \right] \end{array} \right\}$$

$$\dot{S}_{23} = 2C_{2323}(1-D_{22})(1-D_{33})*\left[\dot{E}_{23} - \omega\left(S_{23}\,\tfrac{2L}{(1-D_{22})(1-D_{33})}\right)\right]$$

$$\dot{S}_{13} = 2C_{1313}(1-D_{11})(1-D_{33})*\left[\dot{E}_{13} - \omega\left(S_{13}\,\tfrac{2M}{(1-D_{33})(1-D_{11})}\right)\right]$$

$$\dot{S}_{12} = 2C_{1212}(1-D_{11})(1-D_{22})*\left[\dot{E}_{12} - \omega\left(S_{12}\,\tfrac{2N}{(1-D_{11})(1-D_{22})}\right)\right]$$

B. Determining the Damage Rates

Denote $\boldsymbol{Y} = -\boldsymbol{S} : \left\{\boldsymbol{C}^{-1} : \boldsymbol{M} : \tfrac{\partial \boldsymbol{M}}{\partial \boldsymbol{D}}\right\}^{sym} : \boldsymbol{S}$

$$\begin{aligned}
Y_{11} = &-\left[S_{11} * C^{-1}_{1111} * M_{1111} * dM_{111111} * S_{11}\right] \\
&-\left[S_{22} * \tfrac{1}{2}\left(C^{-1}_{1122} * M_{2222} * dM_{222222} * S_{11} + C^{-1}_{2211} * M_{1111} * dM_{111111} * S_{11}\right)\right] \\
&-\left[S_{33} * \tfrac{1}{2}\left(C^{-1}_{1133} * M_{3333} * dM_{333333} * S_{11} + C^{-1}_{3311} * M_{1111} * dM_{111111} * S_{11}\right)\right]
\end{aligned}$$

$$\begin{aligned}
Y_{22} = &-\left[S_{11} * \tfrac{1}{2}\left(C^{-1}_{1122} * M_{2222} * dM_{222222} * S_{22} + C^{-1}_{2211} * M_{1111} * dM_{111111} * S_{22}\right)\right] \\
&-\left[S_{22} * C^{-1}_{2222} * M_{2222} * dM_{222222} * S_{22}\right] \\
&-\left[S_{33} * \tfrac{1}{2}\left(C^{-1}_{3322} * M_{2222} * dM_{222222} * S_{22} + C^{-1}_{2233} * M_{3333} * dM_{333333} * S_{22}\right)\right]
\end{aligned}$$

$$\begin{aligned}
Y_{33} = &-\left[S_{11} * \tfrac{1}{2}\left(C^{-1}_{1133} * M_{3333} * dM_{333333} * S_{33} + C^{-1}_{3311} * M_{1111} * dM_{111111} * S_{33}\right)\right] \\
&-\left[S_{22} * \tfrac{1}{2}\left(C^{-1}_{3322} * M_{2222} * dM_{222222} * S_{33} + C^{-1}_{2233} * M_{3333} * dM_{333333} * S_{33}\right)\right] \\
&-\left[S_{33} * \left(C^{-1}_{3333} * M_{3333} * dM_{333333} * S_{33}\right)\right]
\end{aligned}$$

$$Y_{23} = -\left[S_{23} * \left(2C^{-1}_{2323} * M_{2323} * dM_{232333} * S_{33} + 2C^{-1}_{2323} * M_{2323} * dM_{232322} * S_{22}\right)\right]$$

$$Y_{13} = -\left[S_{13} * \left(2C^{-1}_{1313} * M_{1313} * dM_{131333} * S_{33} + 2C^{-1}_{1313} * M_{1313} * dM_{131311} * S_{11}\right)\right]$$

$$Y_{12} = -\left[S_{12} * \left(2C^{-1}_{1212} * M_{1212} * dM_{121222} * S_{22} + 2C^{-1}_{1212} * M_{1212} * dM_{121211} * S_{11}\right)\right]$$

The characteristic tensor for plastic damage is defined as L^{d}_{ijkl}

such that $L^{d}_{ijkl} = \eta\delta_{ij}\delta_{kl} + \tfrac{1}{2}(1-\eta)(\delta_{ik}\delta_{jl} + \delta_{il}\delta_{jk})$

$$\boldsymbol{L}^d = \begin{pmatrix} 1 & \eta & \eta & 0 & 0 & 0 \\ \eta & 1 & \eta & 0 & 0 & 0 \\ \eta & \eta & 1 & 0 & 0 & 0 \\ 0 & 0 & 0 & \frac{1}{2}(1-\eta) & 0 & 0 \\ 0 & 0 & 0 & 0 & \frac{1}{2}(1-\eta) & 0 \\ 0 & 0 & 0 & 0 & 0 & \frac{1}{2}(1-\eta) \end{pmatrix}$$

$$\boldsymbol{L}^d : \boldsymbol{Y} = \begin{pmatrix} 1 & \eta & \eta & 0 & 0 & 0 \\ \eta & 1 & \eta & 0 & 0 & 0 \\ \eta & \eta & 1 & 0 & 0 & 0 \\ 0 & 0 & 0 & \frac{1}{2}(1-\eta) & 0 & 0 \\ 0 & 0 & 0 & 0 & \frac{1}{2}(1-\eta) & 0 \\ 0 & 0 & 0 & 0 & 0 & \frac{1}{2}(1-\eta) \end{pmatrix} \begin{pmatrix} Y_{11} \\ Y_{22} \\ Y_{33} \\ Y_{23} \\ Y_{13} \\ Y_{12} \end{pmatrix} = \begin{pmatrix} Y_{11} + \eta\left(Y_{22} + Y_{33}\right) \\ Y_{22} + \eta\left(Y_{11} + Y_{33}\right) \\ Y_{33} + \eta\left(Y_{11} + Y_{22}\right) \\ \frac{1}{2}(1-\eta)Y_{23} \\ \frac{1}{2}(1-\eta)Y_{13} \\ \frac{1}{2}(1-\eta)Y_{12} \end{pmatrix}$$

Now find

$$\boldsymbol{Y} : \boldsymbol{L}^d : \boldsymbol{Y} = \begin{pmatrix} Y_{11} & Y_{22} & Y_{33} & Y_{23} & Y_{13} & Y_{12} \end{pmatrix} \begin{pmatrix} Y_{11} + \eta\left(Y_{22} + Y_{33}\right) \\ Y_{22} + \eta\left(Y_{11} + Y_{33}\right) \\ Y_{33} + \eta\left(Y_{11} + Y_{22}\right) \\ \frac{1}{2}(1-\eta)Y_{23} \\ \frac{1}{2}(1-\eta)Y_{13} \\ \frac{1}{2}(1-\eta)Y_{12} \end{pmatrix}$$

$$= Y_{11}^2 + Y_{22}^2 + Y_{33}^2 + \eta Y_{11}\left(Y_{22} + Y_{33}\right) + \eta Y_{22}\left(Y_{11} + Y_{33}\right) + \eta Y_{33}\left(Y_{11} + Y_{22}\right) + \tfrac{1}{2}(1-\eta)Y_{23}^2 + \tfrac{1}{2}(1-\eta)Y_{13}^2 + \tfrac{1}{2}(1-\eta)Y_{12}^2$$

$$Y_{eq} = (\tfrac{1}{2}\boldsymbol{Y} : \boldsymbol{L}^d : \boldsymbol{Y})^{1/2}$$

$$= \left[\frac{1}{2} \left[\begin{array}{l} Y_{11}^2 + Y_{22}^2 + Y_{33}^2 \\ +\eta Y_{11}\left(Y_{22} + Y_{33}\right) + \eta Y_{22}\left(Y_{11} + Y_{33}\right) + \eta Y_{33}\left(Y_{11} + Y_{22}\right) \\ + \tfrac{1}{2}(1-\eta)Y_{23}^2 + \tfrac{1}{2}(1-\eta)Y_{13}^2 + \tfrac{1}{2}(1-\eta)Y_{12}^2 \end{array} \right] \right]^{1/2}$$

The damage rates may be calculated as follows

$$\dot{D}_{11} = \omega_d \left(L : Y \right)_{11}$$

$$\dot{D}_{22} = \omega_d \left(L : Y \right)_{22}$$

$$\dot{D}_{33} = \omega_d \left(L : Y \right)_{33}$$

$$\dot{D}_{23} = \omega_d \left(L : Y \right)_{23}$$

$$\dot{D}_{13} = \omega_d \left(L : Y \right)_{13}$$

$$\dot{D}_{12} = \omega_d \left(L : Y \right)_{12}$$

where

$$\omega_d = -\frac{1}{2Y_{eq}} \gamma_d \left(\frac{Y_{eq}}{Y_0} \right)^{1/n}$$